Evolution of the Josephine Peridotite shear zones, Part 1: Compositional variation and shear initiation

Kathryn M. Kumamoto[1,2*], Jessica M. Warren[3], Erik H. Hauri[4†]

[1] Department of Earth Sciences, University of Oxford, UK.

[2] Department of Geological Sciences, Stanford University, CA.

[3] Department of Geological Sciences, University of Delaware, DE.

[4] Department of Terrestrial Magnetism, Carnegie Institution of Washington, DC.

[*] Corresponding author, kathryn.kumamoto@earth.ox.ac.uk.

[†] Dr. Erik Hauri contributed substantially to this work before his passing on September 5, 2018.

Key points:

- Ductile shear zones in the Josephine Peridotite, SW Oregon, record a complex history of melting and melt-rock interaction.
- Peridotite hydration, based on orthopyroxene, took place at temperatures greater than 690°C, thus the source of water was most likely melt.
- Initial shear localization in the Fresno Bench outcrop was controlled by the presence of melt and elevated water concentrations.

Abstract

Shear localization in the upper mantle, a necessity for plate tectonics, can have a number of causes, including shear heating, the presence of melt, the development of a strong crystal-preferred orientation, and the presence of water. The Josephine Peridotite of southwestern Oregon contains shear zones that provide an excellent opportunity to examine the initiation of shear localization. These shear zones are relatively small-scale and low-strain compared to many shear zones in peridotite massifs, which typically have extreme grain size reduction indicating extensive deformation. We use major, trace, and volatile element analyses of a large suite of harzburgites from the Fresno Bench shear zones to evaluate the mechanisms leading to shear localization. Lithological evidence and geochemical transects across three shear zones show a complex history of melting, melt addition, and melt-rock interaction. The distribution of aluminum and heavy rare earth elements across the shear zones suggest that melt flow was focused in the centers of the studied shear zones. Water concentrations in orthopyroxene grains of 180–334 ppm H_2O indicate a comparatively high degree of hydration for nominally anhydrous minerals. The correlation of water with aluminum and ytterbium in orthopyroxene is consistent with a melt source for this hydration, suggesting that water equilibrated between the melt and peridotite. The presence of melt and hydration of the host rock provide mechanisms for initial weakening that lead to localized deformation.

1. Introduction

Shear localization is necessary for both the initiation and the continuation of plate tectonics, as it allows the formation of plates with deformation largely confined to the edges (e.g., Bercovici, 2003; Bercovici & Ricard, 2012; Moresi & Solomatov, 1998; Regenauer-Lieb et al., 2001; Tackley, 1998; Trompert & Hansen, 1998). Many hypotheses exist for how shear zones initiate and localize during deformation, including a) shear heating (e.g., Regenauer-Lieb et al., 2001), b) development of a crystal-preferred orientation (CPO) well-aligned for shear (e.g., Tommasi et al., 2009), c) high water concentrations (e.g., Kohlstedt, 2006), d) grain size reduction (e.g., Drury et al., 1991), e) the presence of melt (e.g., Dijkstra et al., 2002; Kelemen & Dick, 1995), and f) spatial variations in the abundance of strong and weak phases (e.g., Dygert et al., 2019; Handy, 1990).

Understanding the initial source of strain localization, however, is difficult as the early stages of this process are rarely preserved. While mylonites are the result of localized deformation, the intense grain size reduction that they have undergone means that only traces of the earlier deformation stages are retained (e.g., Trouw et al., 2009).

The Josephine Peridotite in the western Klamath Mountains of Oregon, USA, is a unique natural laboratory for studying mantle deformation and the mechanisms leading to shear localization, as it contains many small shear zones (ranging in width from 10 cm to 50 m) with limited grain size reduction (Figure 1). The relatively low level of deformation observed in these shear zones offers the opportunity to learn more about the initiation and early evolution of localized deformation. An earlier study in the Josephine Peridotite (Skemer et al., 2013) found that the water content in orthopyroxene was higher in the centers of two of the shear zones relative to their edges. Since the presence of water as H^+ ions in nominally anhydrous minerals like olivine reduces viscosity (for a discussion, see Kohlstedt, 2006), this observation formed the basis of a model that combined water weakening and viscous anisotropy to explain localization in these shear zones. However, only four samples were analyzed in Skemer et al. (2013) and other trace elements were not analyzed.

The presence of melt has also been invoked to explain shear localization in the Josephine Peridotite shear zones (Kelemen & Dick, 1995), as well as other mantle shear zones (e.g., Higgie & Tommasi, 2012, 2014; Kaczmarek & Müntener, 2008; Kruckenberg et al., 2013). Melt can contribute to shear localization at many spatial scales, from the kilometer-scale of plagioclase infiltration in lherzolite of the Lanzo peridotite massif (Higgie & Tommasi, 2014; Kaczmarek & Müntener, 2008) to the centimeter- to millimeter-scale localization along the boundaries of dunite channels in the Twin Sisters ultramafic complex (Kruckenberg et al., 2013). In the Josephine Peridotite, where shear zones are typically identified at the meter-scale, syn-deformational melt flow along dunite channels in the center of shear zones was suggested as the dominant localization mechanism by Kelemen and Dick (1995). Skemer et al. (2013) also cited central melt channels as the source of the elevated water concentrations they observed at shear zone centers, though they considered melt to have an otherwise negligible role in shear localization.

To further evaluate shear localization in the Fresno Bench shear zones, we examined the major, trace, and volatile element composition of three Josephine shear zones in detail: Shear Zone P (SZP), Shear Zone G (SZG), and Shear Zone A (SZA). These three subparallel shear zones are

among the best-exposed in the Fresno Bench outcrop. The microstructures of all three shear zones are closely examined in a companion study (Kumamoto et al., in revision), as well as previous work (Hansen & Warren, 2015; Recanati et al., 2012; Skemer et al., 2010; Warren et al., 2008). Our dataset indicates that the relationship between water and shear localization is more complex than previously estimated. In addition, our results indicate that melt was present in the peridotite as both diffuse and channelized flow. We show that these melts played an important role in localizing deformation and controlling mineral chemistry, particularly in the centers of shear zones.

2. Geological setting

The Josephine Peridotite is the mantle section of a dismembered Jurassic magmatic arc and subsequent back-arc basin (Dick, 1976; Harper, 1984; Saleeby et al., 1982). The massif was emplaced through thrust-faulting over a mafic batholith, producing the present-day east-dipping thrust sheet structure (Garcia, 1982; Harper et al., 1990; Saleeby et al., 1982). The predominant rock type is clinopyroxene-poor (<1%) harzburgite. Incipient hydrothermal alteration is present in the form of serpentine, tremolite, and talc, but overall the massif is composed of relatively fresh peridotite (e.g., Coulton et al., 1995; Dick, 1977; Himmelberg & Loney, 1973).

Fresno Bench – a glacial step 0.5 km in width – has been the focus of mantle deformation studies in the Josephine Peridotite due to the presence of >10 small-scale shear zones (Kelemen & Dick, 1995; Loney & Himmelberg, 1976; Warren et al., 2008). At most peridotite localities on Earth, strain cannot be measured due to the lack of a strain marker in this relatively coarse-grained (>0.5 mm), anhedral lithology. In the Fresno Bench outcrop, however, strain can be determined due to the presence of a pyroxene foliation in some sections, which stands out on the outcrop surface due to the preferential weathering of olivine (Himmelberg & Loney, 1973). Changes in foliation orientation provide a strain marker (Ramsay & Graham, 1970; Warren et al., 2008).

The harzburgite host rock of the Fresno Bench outcrop is cross-cut by various features associated with multiple generations of melt addition and melt-rock interaction, including gabbro veins, olivine websterite veins, orthopyroxenite veins, and dunites (e.g., Dick, 1977; Harper, 1984; Himmelberg & Loney, 1973; Kelemen & Dick, 1995). The contact between dunite and harzburgite is irregular at the sub-centimeter scale, which is texturally consistent with formation of the dunites

by reactive porous flow (Kelemen et al., 1995). In contrast, most of the gabbro and pyroxenite veins have sharp boundaries with the harzburgite. This suggests fracture-driven propagation of melt through the harzburgite, rather than melt actively reacting with the matrix as it flows. These veins are thus interpreted as representing melts that formed elsewhere (e.g., Dick 1976, 1977), though recent experiments have shown that sharp-sided orthopyroxenites can form by reaction between peridotite and hydrous basaltic andesite (Wang et al., 2016).

Establishing the relative timing of events in Fresno Bench is difficult as cross-cutting relationships between the shear zones and the different types of melt features are not consistent across the outcrop. In addition, the lack of continuous bedrock exposure means that many key features can only be followed for short distances. In general, though, olivine websterites represent an early generation of melt and are locally replaced by small dunite pods. In some sections, the pyroxene foliation grades into olivine websterite, and Kelemen and Dick (1995) hypothesized that the foliation could represent olivine websterite transposed during horizontal extension. Skemer et al. (2013) similarly inferred that the foliation was created during mantle upwelling and corner flow. Gabbro and orthopyroxenite typically crosscut the foliation as well as the dunites, with orthopyroxenite usually considered the latest generation of melt as veins of orthopyroxenite crosscut shear zones (e.g., Dick 1976, 1977). In some cases, however, orthopyroxenite is deformed in shear zones (e.g., Skemer et al., 2010).

3. Methods

3.1. Field measurements and sampling

Sample locations for transects across SZA, SZG, and SZP are shown in Figure 2 as cross-section traverses perpendicular to the shear plane orientation. Samples from SZG and SZP are described in Skemer et al. (2010) and Warren et al. (2008), respectively. Samples from SZA include both samples described in Recanati et al. (2012) as well as new samples gathered for this study.

For the new SZA data in this study, measurements of the strike and dip of pyroxene foliations were taken at 40 points in a transect across this shear zone. The shear plane was defined as the foliation plane in the mylonite at the center of the shear zone, and the shear direction was determined from the lineation defined by orthopyroxene grains in the field. To construct a structural cross section,

these field measurements were rotated and projected onto the plane 315/50, which contains the shear direction (trend of 45˚N and plunge of 50˚), and is perpendicular to the shear plane orientation (strike of 45˚N and dip of 90˚). In Figure 2, the x-axis is parallel to the shear direction, and the y-axis is the pole to the shear plane. The transect is shown with the most deformed sample located at the origin. (See supplemental material for a description of the methodology for performing the rotation and projection of field data into a structural cross-section.) Shear strain was calculated based on the two-dimensional deflection of the pyroxene foliation assuming simple shear (Ramsay, 1980; Ramsay & Graham, 1970; Warren et al., 2008) and is reported for each sample in Table S1.

3.2. Electron microprobe analysis

Major element compositions for olivine, orthopyroxene, and spinel were determined using the JEOL JXA-8230 SuperProbe electron probe microanalyzer at Stanford University. Samples and thin sections were polished to at least 1 μm smoothness and carbon coated prior to analysis. The probe current was maintained at 20 nA for orthopyroxene and 30 nA for olivine and spinel using a 15 kV beam. In order to account for the exsolution present in pyroxene, each orthopyroxene grain was measured using a 10 μm spot size at 10 μm intervals along a 100 μm transect perpendicular to exsolution, which was visible in the backscattered electron image. A 2 μm spot size was used to analyze olivine and spinel, with 3–5 points collected per phase. A linear background correction was used for each element and the ZAF procedure (Armstrong, 1988) applied for matrix correction. Spinel compositions were determined using the methods and spinel standards detailed in Davis et al. (2017), which allows for the accurate determination of both Fe_2O_3 and FeO concentrations. TiO_2 background measurements were incorrect during spinel analyses, but concentrations are estimated to be below 0.5 wt%. Individual points of any phase with totals above 101.5 or below 98.5 indicate poor quality analyses and were excluded from the dataset.

3.3. Laser ablation inductively coupled plasma mass spectrometry (LA-ICPMS)

Trace elements were measured in orthopyroxene grains from samples across all three shear zones using a Thermo Fisher iCAP Q equipped with a Photon Machines 193 Excimer laser at the Carnegie Institution of Washington. Samples were run at a 20 Hz laser repeat rate for 400-800

shots, with ~20 seconds of gas blank measurement at the start of every analysis. The laser spot size was 95 μm. Standards BCR-2G, BHVO-2G, BIR-1G, KL2-G, ML-3B-G, GSC, GSA, GOR-132-G, GOR-128-G, and BM90-21-G (Jochum et al., 2005, 2006) were run approximately every 30 analyses to account for drift. Data were processed using the Lasyboy Excel macro, written by Joel Sparks at Boston University. Individual elements that are below detection or that accumulated counting errors greater than 60% were filtered out of the dataset.

3.4. Secondary ion mass spectrometry (SIMS)

Water, fluorine, and phosphorus concentrations were measured in olivine and orthopyroxene grains using the Cameca IMS Secondary Ion Mass Spectrometer at the Carnegie Institution of Washington over two sessions in 2014. Clinopyroxene was not analyzed as this phase is only present in trace amounts in the Fresno Bench harzburgites. Gold-coated samples were analyzed using a rastered Cs^+ beam with a current of 15–25 nA. An electron flood gun was used to charge balance the raster area. The sputter pits were typically 30–40 μm in diameter, but only the center 10 μm were analyzed by inserting the smallest field aperture. Measurements of carbon, sulphur, and chlorine, as well as the variability in water counts at each individual SIMS spot, were used to detect contamination or interference from inclusions and hydrous phases. Grains of Suprasil 3002 glass and ALV-519-4-1 basaltic glass were measured every 10-20 analyses to track background water content and calibration drift, respectively, following the methods described in Kumamoto et al. (2017).

Working curves were constructed using standards calibrated by Koga et al. (2003) and Aubaud et al. (2007). Orthopyroxene standards for measuring water were Opx A288, India Enstatite, KBH-1, and ROM-273-OG2 and were run at the beginning of each analytical session. Since olivine and orthopyroxene have near-identical calibration slopes (Koga et al., 2003; Kovacs et al., 2010; Mosenfelder & Rossman, 2013; Warren & Hauri, 2014; Withers et al., 2011), the orthopyroxene standards were also used for data reduction on olivine. Basaltic glass standards were used to construct a working curve for fluorine and phosphorus as matrix-matched standards do not yet exist for these elements. These glasses, calibrated by Hauri et al. (2002), were ALV-519-4-1, WOK-28-3, ALV-1654-3, ALV-1833-1, ALV-1833-11, and ALV-1846-12. The values used for these standards can be found in Kumamoto et al. (2017).

4. Results

4.1. Lithological observations of pre- and syn-deformational melt features

We identified melt interaction features in each of the three shear zones studied. The center of SZG contains deformed orthopyroxenite veins that are aligned with the foliation and are boudinaged and partially recrystallized (Figure 3a). The occurrence of boudins indicates that the veins were more viscous than the host rock during deformation and therefore must have been crystalline (Skemer et al., 2010, 2013). While the SZA transect presented here does not contain macroscopic evidence of melt, plagioclase occurs interlayered at the mm-scale with harzburgite in the shear zone center ~80 m along strike of our transect (Figure 3b). This is similar to the observations of plagioclase in the Lanzo peridotite massif (e.g., Kaczmarek & Müntener, 2008) but at a much smaller scale. The presence of dispersed plagioclase within the harzburgite over a width of ~0.4 m in the center of the shear zone is best explained by the presence of a syn-deformational gabbroic melt. Finally, in SZP (Figure 3c), a central irregular dunite pod on strike with the shear plane is interpreted as a central melt channel associated with shear zone formation (Kelemen & Dick, 1995). Unlike observations in the Twin Sisters ultramafic complex (Kruckenberg et al., 2013), we do not observe any offset between the harzburgite and dunite, suggesting that deformation was not localized along the dunite channel boundaries.

4.2. Major element chemistry

Major element compositions for olivine, orthopyroxene, and spinel are given in Tables S2–S4 as the average of multiple points per sample. The forsterite number (Fo#) of olivine ranges from 90.9 to 91.7, similar to the range seen for the Josephine Peridotite overall (89.6–91.9; Dick, 1977, Le Roux et al., 2014). Spinel chrome number ranges from 47.6 to 53.2, in agreement with previous analyses of samples from Fresno Bench (Morgan et al., 2008), while the range for the Josephine Peridotite overall is ~15 to ~80 (Dick, 1977; Dick & Bullen, 1984; Le Roux et al., 2014). The Fresno Bench samples plot at the more refractory end of spinel and olivine compositional trends for peridotites (Figure 4).

4.3. Trace elements

Concentrations of 38 minor and trace elements measured in orthopyroxene are reported in Table S5. Clinopyroxene was not measured as it is virtually absent in all samples. Trace element patterns are normalized to Primitive Upper Mantle values (PUM; Palme & O'Neill, 2014) in Figure 5a. Rare earth element (REE) patterns for the same samples are depicted in Figure 5b, normalized to chondrite (Anders & Grevesse, 1989), following the convention for REE datasets.

The Fresno Bench samples generally have low concentrations of trace elements, with many of the more incompatible elements below detection (Figure 5, Table S5). Compared to data from Le Roux et al. (2014), which provide constraints on the overall composition of the Josephine Peridotite, the Fresno Bench orthopyroxenes generally have low abundances of REEs (Figure 5b). The depletion in the middle- and heavy-REEs (MREEs and HREEs, respectively) indicates that the samples have undergone extensive fractional melting (e.g., Johnson et al., 1990). Similarly, the Fresno Bench samples plot at the depleted end of the orthopyroxene Yb versus spinel Cr# trend (Figure 4c).

Within each shear zone, one or two harzburgites have chemical profiles that vary significantly from the patterns expected from melt depletion. Elevated concentrations of LREEs and other highly incompatible elements compared to other samples from the shear zones are present in JP10-M13 in SZA, 3925-G05 and 3925-G02 in SZG, and 3924-J09a and 3924-J10 in SZP (Figure 5b). In addition, orthopyroxene from sample 3924-J06 in SZP is extremely refractory, with depletions in the moderately incompatible elements (Gd–Lu) relative to all other samples (Figure 5b). These enrichments and extreme depletions do not vary systematically with strain. For example, the only sample from SZA with elevated LREE abundances is JP10-M13, which has a relatively low strain of 0.31. As discussed below, these compositional features are all characteristic of high degrees of melt extraction, with minor amounts of melt addition in some samples.

4.4. Volatile concentrations

Water concentrations in the shear zones vary from 180 to 334 ppm H_2O in orthopyroxene (Table S6). Olivine water concentrations for 11 samples from across these shear zones range from 4–17 ppm (Table S7). Based on the experimentally-constrained water partition coefficient ($D^{ol/opx}$) of 0.11 (Aubaud et al., 2004; Hauri et al., 2006; Tenner et al., 2009), the two phases appear to be out

of equilibrium. Olivine is relatively dry, similar to previous observations of water concentrations in these coexisting phases (e.g., Peslier, 2010; Warren & Hauri, 2014), though some studies of natural samples have suggested that $D^{ol/opx}$ may be lower than determined experimentally (e.g., Grant et al., 2007).

One of the most striking aspects of the Fresno Bench dataset is the covariation of water with moderately incompatible elements including aluminum, chromium, HREEs, and MREEs in orthopyroxene. These covariations are illustrated for H_2O, Al_2O_3, Gd, and Yb in Figure 6. Correlations with MREEs (e.g., Gd) are less systematic than with HREEs (e.g., Yb).

Transects of orthopyroxene water concentration versus distance across each shear zone are shown in Figure 7a. In these transects, distance from the shear plane is calculated parallel to the shear plane normal using the structural cross-section constructed for each shear zone (Figure 2). At the edges of the shear zones, orthopyroxene has an average water content of 255 ± 25 ppm H_2O (n=13). Water concentrations do not vary in the shear zones relative to this "regional" concentration until moderate strains >1.5 (~5 m away from the center of the shear zone in SZA and SZP; see Figure 2 and Table S1 for sample strains) in all three shear zones (Figure 7a).

In SZA and SZP, samples that have undergone higher strain exhibit both higher and lower water contents relative to the ~260 ppm H_2O observed in the low-strain samples. Samples with the highest strain have low water contents: JP10-M08 in SZA has 194 ± 10 ppm H_2O and 3924-J08 in SZP has 214 ± 13 ppm. However, samples with the highest water contents occur only 1–5 meters away and also underwent high strain: JP10-M06 and JP14-D06 in SZA have 334 ± 14 ppm and 322 ± 18 ppm respectively, while 3924-J10 in SZP has 312 ± 29 ppm. The water concentration transects for these two shear zones are remarkably similar to one another (Figure 7a). In contrast, water concentrations in SZG, the narrowest of the shear zones with the greatest grain size reduction, are relatively constant across the entire shear zone.

Transects of the moderately incompatible elements across the three shear zones have spatial features that are similar to the water transects (Figure 7b, 7c). As with water, the highest strain samples in SZA and SZP have relatively low concentrations of moderately incompatible elements, but nearby samples with high strains have comparatively high concentrations of these elements.

Fluorine and phosphorus are above detection in the Fresno Bench shear zones, ranging from 0.02–2.02 ppm F and 0.2–6.8 ppm P (Table S6). Concentrations of these two elements versus distance

(Figure S1) reveal no discernable systematic variation in the abundance of either element as a function of strain or major element chemistry.

5. Discussion

5.1. Melting and melt-rock interaction in the shear zones

5.1.1. Estimated degree of fractional melting in Fresno Bench

Several aspects of the peridotite geochemistry at Fresno Bench imply a high degree of fractional melting. The presence of harzburgite with very little clinopyroxene requires a significant amount of melting in order to remove nearly all clinopyroxene. Based on the trend in spinel Cr# versus spinel Mg# and olivine Fo# (Figure 4), where higher values of spinel Cr# and olivine Fo# and lower values of spinel Mg# reflect greater melt extraction (Arai, 1987, 1994; Dick & Bullen, 1984), the Fresno Bench samples plot at the refractory end of the global abyssal peridotite array. In addition, moderately incompatible trace elements (e.g., HREEs) in orthopyroxene are depleted relative to estimated source mantle and co-vary with spinel Cr# (Figure 4c).

To estimate the degree of melting, we used the nonmodal fractional melting reference model of Warren (2016), assuming Depleted MORB Mantle (DMM; Workman & Hart, 2005) as the initial composition and using partition coefficients from Kelemen et al. (2003) and Sun and Liang (2014). The HREEs in our orthopyroxenes are well-matched by 16–18% melting (Figure 8). This amount of depletion is consistent with the general lack of clinopyroxene in peridotites from Fresno Bench, as clinopyroxene is melted out of peridotite at ~18% melting in this model. In contrast, samples from elsewhere in the Josephine Peridotite can be approximately fit by as little as 8% melting (Figure 8).

5.1.2. Modeling melt-rock interaction

Fractional melting is a theoretical end-member model that assumes instantaneous removal of melt from the peridotite. This model is useful for providing an estimate of the degree of melting recorded by moderately incompatible trace elements such as the HREEs. However, the chemical composition of the host peridotite is often changed due to interactions with melt fluxing through

the system, as reflected by deviations of highly incompatible elements (such as the LREEs) from the fractional melting model (Birner et al., 2017; Brunelli et al., 2006; Hellebrand et al., 2002). At Fresno Bench, we found compositional effects ranging from macroscopic veins to subtle trace element enrichments that we interpret as evidence for melt-rock interaction across a variety of length-scales.

In SZG, the minor LREE enrichments in 3925-G02 and 3925-G05 relative to most of the Fresno Bench samples could be related to the presence of the orthopyroxenite veins, but the enrichments in samples from SZA (JP10-M13) and SZP (3924-J09a and 3924-J10) are not associated with visible veins in outcrop. Elevated LREEs in pyroxenes have previously been attributed to late-stage, low-volume melt refertilization (Birner et al., 2017; Bodinier et al., 1990; Brunelli et al., 2006; Hellebrand et al., 2002; Navon and Stolper, 1987; Vernières et al., 1997; Warren, 2016). In the Fresno Bench shear zones, we interpret harzburgites with elevated abundances of highly incompatible elements to have undergone interaction with small amounts of melt that flowed through the harzburgite during melt extraction.

To model the trace element enrichments that we observe in the Fresno Bench samples, we use the closed-system, melt refertilization model developed by Birner et al. (2017). This model is based on a simple minimization scheme to optimize (1) the degree of fractional melting from a DMM source and (2) the amount of melt added in order to match observed trace element concentrations. We use the average E-MORB composition in Gale et al. (2013) as a first-order estimate for the melt composition, though many different melt compositions are possible in a suprasubduction zone setting (e.g., Mullen et al., 2017). The LREEs in the five enriched Fresno Bench samples can be reasonably well-fit by ≤0.03% added melt after 16–18% fractional melting (Figure 9) while modeling the chemistry of samples without LREE enrichment requires incorporating <0.001% added melt.

The combination of fractional melting and melt addition in the Birner et al. (2017) model fits the REEs fairly well in all of the Fresno Bench samples. The one exception is the extremely refractory harzburgite 3924-J06, which has lower MREE and HREE abundances than all other samples in this study and thus requires a greater degree of fractional melting than the maximum possible partial melting currently provided by the model. Our calculations also underestimate the fluid mobile elements (Ba, Pb, and Sr) for most samples. These elements are extremely sensitive to the

composition of the added melt, and further refinement of the melt composition, including the use of subduction-related melts, would improve the fit between the model and fluid mobile elements.

While the simple melt addition model can explain the enriched LREEs, it doesn't capture the range of covariation that we observe among the moderately incompatible elements (e.g., Figure 6). Instead, these covariations would likely be better fit by an open-system melting model. In open-system melting, the host peridotite is interacting with a fluxing melt while melting, which allows for continual reequilibration between melt and peridotite. Modeling this type of interaction requires that assumptions be made about many parameters, including porosity, permeability, melt composition, and melt addition rate. In general, open-system models have found that allowing melt flux during melting leads to increased concentrations of incompatible elements (Brunelli et al., 2014; Godard et al., 2008; Vernières et al., 1997). Open-system melting has been used to explain peridotites with high ratios of very incompatible elements like LREEs compared to moderately incompatible elements like HREEs (e.g., Brunelli et al., 2014; Godard et al., 2008). Thus, in addition to explaining the five Fresno Bench samples with LREE enrichments, open-system melting may also explain the detectable LREEs in the other samples.

5.1.3. Importance of the Fresno Bench trace element variations

Our analysis of Fresno Bench reveals two types of melt-rock interaction: channelized flow (e.g., dunites and veins), and diffuse flow (e.g., trace element enrichments away from visible veins). Previous studies that have explored geochemical changes associated with melt transport in the mantle have focused on channelized flow in the form of with dunite pods and pyroxenite veins (e.g., Bodinier et al., 1990; Borghini et al., 2013; Dygert et al., 2016; Morgan et al., 2008; Suhr et al., 2003). These studies found that peridotite immediately next to melt channels was chemically affected by processes associated with the melt channel, exhibiting either enrichment (e.g., Bodinier et al., 1990) or depletion (e.g., Dygert et al., 2016) of the host peridotite around the channel.

Our high-resolution sampling demonstrates that re-enrichment occurs in harzburgite away from visible melt channels. While the shear zones in this study are each associated with some type of melt feature (Figure 3), samples with enriched LREEs have no spatial correlation with these features, and they look no different petrographically than the harzburgite samples on either side of them. These observations suggest that diffuse melt-rock interaction occurs in the harzburgites, in addition to the channelized melt flow represented by dunites, pyroxenites, and gabbros. Our dataset

provides an important constraint for reactive melt transport models (e.g., Keller & Katz, 2016), as it demonstrates the compositional range induced in the trace element signature of the residue due to diffuse melt transport.

5.2. Melt-rock interaction as the source of water concentrations and variations

Having evaluated the role of melt in producing the REE variations in the Fresno Bench shear zones, we now evaluate the origin of the water variations in the shear zones. The covariation seen between water and the moderately incompatible elements (e.g., Figure 6) suggests that water concentrations, as well as aluminum and chromium concentrations, were controlled by the same processes governing the REE concentrations: melt depletion and melt-rock interaction. We propose that the variation in water in the Fresno Bench orthopyroxenes is controlled by the solubility of water in orthopyroxene, which is dependent on major element chemistry, which in turn is controlled by melt-rock interaction.

5.2.1. Calculating potential hydration conditions

To assess possible hydration conditions for the Fresno Bench orthopyroxenes, we use the observed relationship between trivalent cations and water in our samples to calculate the concentration of water in enstatite. Experiments on water solubility in orthopyroxene have found that solubility depends on the concentration of trivalent cations like Al^{3+} (e.g., Rauch & Keppler, 2002; Stalder, 2004; Stalder et al., 2005), in addition to pressure and temperature. Water can be incorporated into aluminous orthopyroxene as hydrogen by coupled substitutions associated with either octahedral or tetrahedral aluminum: $Al^{3+} + H^{+} = 2Mg^{2+}$ and $Al^{3+} + H^{+} = Si^{4+}$ (Stalder, 2004; Stalder et al., 2005). Other trivalent cations like Cr^{3+} and Fe^{3+} can also increase water solubility through similar coupled substitutions, though the presence of multiple trivalent cations can result in dry coupled defects like $Al^{3+} + Cr^{3+} = Mg^{2+} + Si^{4+}$ (Prechtel and Stalder, 2012; Stalder et al., 2005; Stalder et al., 2015). Overall, the water solubility in natural orthopyroxene is much greater than end-member Mg-pyroxene as greater concentrations of trivalent cations increase hydrogen solubility, consistent with the trend in Figure 6a. However, the effect of trivalent cations on solubility has not been quantified experimentally as a function of pressure-temperature conditions.

To calculate a first-order approximation of the concentration of water in enstatite in equilibrium with the Fresno Bench orthopyroxene, we made the following assumptions:

1. We assume that the water concentrations in Fresno Bench orthopyroxenes represent equilibrium values, with different concentrations representing different solubilities due to the variable major element chemistry. We interpret the trend between water and alumina in orthopyroxene (Figure 6a) to record variable solubility of water in orthopyroxene.
2. We assume that octahedral and tetrahedral aluminum both contribute to increased water solubility in orthopyroxene via $Al^{3+} + H^{+} = 2Mg^{2+}$ for octahedral and $Al^{3+} + H^{+} = Si^{4+}$ for tetrahedral.
3. We assume that all the chromium present in the Fresno Bench orthopyroxenes forms Tschermak defects with aluminum ($Cr^{3+} + Al^{3+} = Mg^{2+} + Si^{4+}$). This was observed by Stalder et al. (2005) for Al/(Al+Cr) > 0.6 in enstatite doped with chromium and aluminum, as well as in natural mantle orthopyroxene. On an atoms per formula unit basis, the presence of chromium in addition to aluminum reduces the amount of aluminum available to charge balance water.
4. We assume that the net effect of ferric iron on the solubility of water is negligible in the Fresno Bench orthopyroxenes. While ferric iron is most likely present, we have not measured its concentration in any of the Fresno Bench orthopyroxenes. Other studies that directly measure ferric iron in natural and experimental orthopyroxenes report an average of 4% Fe^{3+} out of the total iron present (Canil & O'Neill, 1996; Malaspina et al., 2012; Stalder et al., 2005). This equates to ~0.5 wt% Fe_2O_3 in the Fresno Bench orthopyroxenes, a concentration on the order of the Cr_2O_3 concentrations. In enstatite doped with iron, Fe^{3+} may be charge-balanced by both water and $Fe^{3+} + Fe^{3+}$ Tschermak defects (Stalder et al., 2005), but the effect of Fe^{3+} on orthopyroxene with multiple types of trivalent cations is not clear.
5. We assume that no Tschermak defects involve only aluminum ($Al^{3+} + Al^{3+}$). While these defects undoubtedly exist, we have no way of quantifying their effect on the water concentrations present in the Fresno Bench samples. The presence of these defects would reduce the amount of aluminum available to charge balance water.

Based on these assumptions, we quantified the effect of aluminum and chromium on water concentration. In Figure 10a, the orthopyroxene water concentrations are plotted against the number of cations of aluminum per formula unit minus the number of chromium ions per formula unit. Extrapolating the linear relationship back to enstatite, where trivalent cations should play a

negligible role in water solubility (i.e., [Al] – [Cr] = 0), the water concentration in orthopyroxene is 62 ppm. We take this concentration to be representative of the water content of end-member enstatite in equilibrium with the water concentrations in the trivalent-cation-bearing orthopyroxenes of Fresno Bench.

Using Rauch and Keppler's (2002) experimentally-calibrated equation for the solubility of water in end-member enstatite,

$$c_{\mathrm{H_2O}} = A(T) f_{\mathrm{H_2O}}^{n} \exp\left(-\frac{P\Delta V_{\mathrm{solid}}}{RT}\right), \quad (1)$$

we calculate solubility over a range of temperatures at pressures associated with the Fresno Bench shear zones (0.3–1.0 GPa; Kelemen & Dick, 1995). In this equation, the solubility of water ($c_{\mathrm{H_2O}}$) is a function of a temperature-dependent constant ($A(T)$), water fugacity ($f_{\mathrm{H_2O}}$), the volume change of the pyroxene structure when water is incorporated ($\Delta V_{\mathrm{solid}}$), pressure ($P$), and temperature ($T$). Using water fugacities obtained from the equation of Pitzer and Sterner (1994), Rauch and Keppler (2002) fit $A(T)$ as 0.0204 ppm/bar and $\Delta V_{\mathrm{solid}}$ as 12.3 cm^3/mol for the fugacity exponent $n = 1$ and a temperature of 1100˚C. Using these values, Figure 10b shows that the solubility of water in enstatite (i.e., the maximum concentration of water possible in enstatite) increases as a function of both pressure and temperature. While increasing pressure at constant water fugacity should decrease the solubility of water in enstatite, the increase in water fugacity with increasing pressure (Pitzer and Sterner, 1994) outweighs this effect.

Orthopyroxene water concentrations must fall either on the solubility surface in Figure 10b (for saturated conditions) or below the solubility surface (for undersaturated conditions). Given that the water fugacities of Pitzer and Sterner (1994) are maximum water fugacities, representing pure water at the given pressure and temperature conditions, this solubility surface is an upper limit of possible saturation conditions—lower water fugacities would shift the entire surface to lower solubilities.

Using our calculation of 62 ppm H_2O in enstatite based on the water content of Fresno Bench orthopyroxene and the pressure estimate of 0.3–1.0 GPa for shear zone formation of Kelemen and Dick (1995), the solubility surface in Figure 10b indicates that hydration occurred at temperatures >690˚C. Thus, assuming all the Fresno Bench orthopyroxenes were hydrated during an outcrop-wide event, temperatures must have been at least 690˚C during hydration. This temperature is

likely an underestimate, as the water fugacity in the mantle was likely lower than that of pure water, and higher hydration temperatures and/or pressures would be necessary to reach 62 ppm H_2O in enstatite. This minimum temperature is consistent with two possible sources of water, either a melt or a hydrothermal fluid.

5.2.2. Evaluating potential sources of water

The water concentrations in the Fresno Bench orthopyroxenes (180–334 ppm H_2O) are too high to be explained by a fractional melting and melt addition model. After the 16–18% fractional melting indicated by the HREEs (Figure 8), orthopyroxene should contain $<10^{-9}$ ppm H_2O. Using the melt refertilization model described above, where a small proportion of melt is mixed back into the peridotite, the addition of 0.03% MORB melt (the proportion of melt addition estimated based on the highest LREE concentrations in Fresno Bench; Figure 9) with 1.5 wt% H_2O (the maximum water concentration measured in MORB by Dixon et al., 2002), results in ~15 ppm H_2O in orthopyroxene. Using an arc melt water content of 4 wt% H_2O (Plank et al., 2013), the addition of 0.03% melt results in only ~40 ppm in orthopyroxene.

An alternative way to evaluate the water contents measured in the orthopyroxenes is to consider equilibrium partitioning with a hydrous melt. This would fit with open-system melting, where melts can be a source or sink for different elements and hydrogen has the potential to decouple from other elements as it diffuses much faster in orthopyroxene (e.g., Carpenter, 2003; Stalder & Behrens, 2006; Stalder & Skogby, 2003). We calculated the predicted equilibrium water content in the melt based on the partition coefficient for water between orthopyroxene and melt ($D^{opx/melt}$). At the Al_2O_3 concentrations observed in the Fresno Bench samples (1.8–3.0 wt% Al_2O_3), $D^{opx/melt}$ ranges from 0.006 to 0.009 (Table S9), using the relationship for $D^{opx/melt}$ as a function of Al_2O_3 observed by Hauri et al. (2006). This corresponds to melt with a water concentration of 2.7–3.9 wt%, which is a reasonable water content for an arc setting (e.g., Plank et al., 2013). Thus, the water concentrations preserved in the Fresno Bench orthopyroxenes are consistent with a hydrous melt fluxing through the outcrop.

The other possible source of water for the Fresno Bench orthopyroxenes is a hydrothermal fluid. Hydrothermal alteration is recorded in the outcrop predominantly in the forms of serpentine and tremolite. Serpentine occurs as cross-cutting veins and as a mesh texture replacing olivine (Figure 1) and is most likely lizardite or chrysotile, as seen elsewhere in the Josephine Ophiolite (Coulton

et al., 1995; Harper et al., 1996; Sonzogni et al., 2017). These low-temperature forms of serpentine are unstable at temperatures greater than ~350˚C (e.g., Evans, 2004; Schwartz et al., 2013) and are therefore unrelated to any hydration at ≥ 690˚C. Tremolite, on the other hand, is present in rims around orthopyroxene grains throughout Fresno Bench and is stable up to ~850˚C at 0.3–1.0 GPa (e.g., Chernosky et al., 1998). Hence, the fluid that caused tremolite alteration could also have hydrated orthopyroxene post-deformation, with the concentration of trivalent cations in orthopyroxene controlling the observed systematic variations in the transects by controlling the solubility of water.

While we cannot rule out the possibility that the source of the water currently present in the Fresno Bench orthopyroxenes was a hydrothermal fluid, we suggest that the relative variations in water concentration are representative of the variations in water concentration during deformation. The covariation of alumina with ytterbium (Figure 6d) strongly indicates that alumina concentrations were set by the melt processes that also set ytterbium concentrations. If water concentrations across the shear zone were in equilibrium during deformation, then the shape of the water transect (Figure 7a) reflects the variations in alumina due to aluminum's strong effect on water solubility. Even if this was later overprinted by a hydrothermal fluid, we suggest that the relative variations in water content were established during melt flow. For the remainder of this paper, we will evaluate the effect of water assuming that current concentrations reflect paleo-concentrations during deformation.

5.3. Geothermometry

Mineral thermometry can be a useful tool for constraining temperature conditions during past processes, including deformation (e.g., Jaroslow et al., 1996; Linckens et al., 2011). In the nearly clinopyroxene-free rocks of the Fresno Bench outcrop, few thermometers are available. We calculate temperatures for our shear zone transects (Figure S2) in two ways using our major element data: the Al/Cr-in-orthopyroxene thermometer of Witt-Eickschen and Seck (1991) and the olivine-spinel thermometer of Li et al. (1995). Both of these thermometers are based on the closure temperatures of major element diffusion in their host mineral(s). As observed in other studies that have applied multiple thermometers (e.g., Birner et al., 2017; Dygert & Liang, 2015; Hidas et al., 2013; Précigout et al., 2017), the temperatures recorded by each thermometer vary systematically,

reflecting differences in closure temperature of the different mineral systems as the peridotite cooled.

In the Fresno Bench shear zone samples, using the Al/Cr-in-opx thermometer results in higher temperatures (1016 ± 33˚C, n = 32) than the olivine-spinel thermometer (900 ± 26˚C, n = 7). While the Fresno Bench samples are outside of the calibration range of the Witt-Eickschen and Seck (1991) thermometer, the thermometer may still be applicable. The temperatures that we calculate are within the range of previous estimates based on other thermometers for the Fresno Bench area (750–1200˚C, Dygert & Liang, 2015; 950–1050˚C, Kelemen & Dick, 1995; 950–1000˚C, Skemer et al., 2010) and other parts of the Josephine Peridotite (900–1100˚C, Harding, 1988; 1000–1200˚C, Himmelberg & Loney, 1973). Estimates from the Al/Cr-in-opx thermometer and the olivine-spinel thermometer do not vary systematically outside of error across the shear zones (Figure S2), indicating that shear heating likely did not play a role in deformation.

Mineral thermometry can be difficult to link to a deformation process as the thermometer closure temperature may not coincide with conditions of deformation. In the Fresno Bench area, we interpret our thermometry estimates as recording the temperature of melt-rock interaction and deformation based on the evidence for syn-deformational melt. Since we concluded above that the major elements in our samples were set by melt-rock interaction during deformation, major-element thermometers should record either the temperature of melt-rock interaction or a lower temperature corresponding to the closure temperature (i.e., the temperature at which diffusion of the exchanging elements is too slow to reach equilibrium). Thus we suggest that the shear zones formed at a minimum temperature of ~1000˚C using the Al/Cr-in-opx thermometer. This temperature estimate is consistent with the high-temperature microstructures and inferred deformation mechanisms of the Fresno Bench shear zones (Kumamoto et al., in revision; Nevitt et al., 2019; Skemer et al., 2010, 2013; Warren et al., 2008). The lower temperature range (900˚C ± 26˚C) given by the olivine-spinel thermometer (Li et al., 1995) is also consistent with these processes. Finally, these temperatures are consistent with melt-rock interaction and hydration by melt as discussed in the previous section.

5.4. Shear initiation in Fresno Bench

The shear zones in Fresno Bench represent the early stages of shear localization in the mantle. The study of Skemer et al. (2013) proposed that these shear zones formed through a combination of water weakening and viscous anisotropy, based on water concentration data for four samples. They suggested that the source of higher water contents in the center of their shear zone model was melt, but they assumed the effect of that melt on viscosity was minimal and did not cause localized weakening. Here we re-assess the roles of melt and water for shear initiation based on our detailed sampling transects across three shear zones (32 samples) and our observations of melt across Fresno Bench.

5.4.1. Effect of melt on viscosity

Our evaluation of the Fresno Bench outcrop and geochemical datasets demonstrates that melt was present prior to and during deformation. For melt to affect shear initiation and localization by creating a viscosity contrast, the melt must be focused, with higher melt fractions at the center of the shear zone (e.g., Holtzman et al., 2003).

To determine the effect of melt on shear initiation, we examined the olivine flow laws for dislocation creep and diffusion creep. Olivine flow laws for these deformation mechanisms can be expressed as

$$\dot{\varepsilon} = A\sigma^n d^{-p} c_{\mathrm{H_2O}}^r \exp(\alpha\phi)\exp\left(-\frac{E^*+PV^*}{RT}\right), \quad (2)$$

where $\dot{\varepsilon}$ is strain rate, A is a pre-exponential term, σ is stress, n is the stress exponent, d is grain size, p is the grain size exponent, $c_{\mathrm{H_2O}}$ is water concentration in ppm H/Si, r is water concentration exponent, α is a constant, ϕ is melt fraction, E^* is the activation energy, P is the pressure, V^* is the activation volume, R is the gas constant, and T is temperature. Flow law parameters (Table S10) are from Hirth and Kohlstedt (2003), with updated values for V^* for dry dislocation creep from N.A. Dixon and Durham (2018) and for A for dry diffusion creep from Hansen et al. (2011).

In these flow laws, the effect of melt on strain rate is formulated as $\dot{\varepsilon} = \exp(\alpha\phi)$, where α has a value of 25–45, as calibrated by experiments (Cooper & Kohlstedt, 1984; Gribb & Cooper, 2000; Hirth & Kohlstedt, 1995a, 1995b; Mei et al., 2002). Assuming $\alpha = 30$, the strain rate in a nominally melt-free sample is a factor of 2.5 lower than in a sample with a melt fraction of 3%, the average

melt fraction estimated to occur during dunite formation (e.g., Braun & Kelemen, 2002; Spiegelman et al., 2001; Spiegelman & Kelemen, 2003). In some areas, our observations indicate that melt fractions can locally exceed 7%, based on our analysis of intermingled plagioclase in peridotite from SZA (Figure 3b). This would lead to the strain rate in the melt-bearing region being a factor of 8 greater than a nominally melt-free region.

Faul and Jackson (2007) presented a flow law for melt-free diffusion creep that is stronger than the Hirth and Kohlstedt (2003) flow law. For melt-free conditions, 300 MPa pressure (the pressure of the experiments performed by Faul and Jackson, 2007), and a differential stress of 15 MPa, strain rates from the Faul and Jackson (2007) flow law are 2.8 orders of magnitude smaller than the original Hirth and Kohlstedt (2003) diffusion creep flow law. This contrast drops to 1.3 orders of magnitude when the Hirth and Kohlstedt (2003) flow law is updated with a value for the pre-exponential term A determined by Hansen et al. (2011) using improved methodology for estimating grain size. Comparing the melt-free flow law of Faul and Jackson (2007) to the updated version of the melt-bearing flow law of Hirth and Kohlstedt (2003), at 300 MPa pressure and a differential stress of 15 MPa, an olivine aggregate with 3% melt would deform 1.7 orders of magnitude faster than a melt-free aggregate with the same grain size. Faul and Jackson (2007) suggested that their melt-free flow law was stronger due to very small amounts of melt in the nominally melt-free experiments of Hirth and Kohlstedt (2003) and that these small melt fractions (<1%) have a large effect on creep. Other studies have also shown that melt fractions as small as 0.01% can affect mechanical properties (Faul et al., 2004; Jackson et al., 2004). Given our observations for the presence of both diffuse and channelized melt flow across the Fresno Bench outcrop, we use the Hirth and Kohlstedt (2003) nominally melt-free diffusion creep flow law in our evaluation of shear localization below.

5.4.2. Effect of water on viscosity

Elevated water concentrations are present in the shear zones (Figure 7a, Table S6), and even small amounts of water can have a major weakening effect in olivine (e.g., Chopra & Paterson, 1984; Hirth & Kohlstedt, 1996; Karato et al., 1986; Kohlstedt, 2006). Determining the exact contribution of water to shear localization is difficult as our water concentration transects (Figure 7a) are complex. Samples with the highest strain (and often the greatest grain-size reduction) do not have the highest water concentrations, though the highest water concentrations are within a few meters

of the samples with the highest strain. In addition, in order to examine the effect of water on deformation of the Fresno Bench samples, we are most interested in how much water was in olivine during deformation, rather than in orthopyroxene. Since olivine has degassed, we rely on experimental constraints for the partitioning of water between olivine and orthopyroxene to predict the syn-deformation water contents. As discussed above, this relies on the assumption that the water in orthopyroxene was present during deformation. In addition, the role of aluminum in olivine is unclear, with some studies suggesting that the presence of aluminum increases the solubility of water in olivine (e.g., Férot & Bolfan-Casanova, 2012), while others suggest that it has a minimal effect compared to the role of other trace elements like titanium (e.g., Tollan et al., 2018). Currently, experimental data are not available to quantify how aluminum or other trace elements in olivine would affect the partitioning of water between olivine and orthopyroxene. We therefore assume that an olivine/orthopyroxene partition coefficient of 0.11 (the average of aluminum-bearing experiments from Aubaud et al., 2004; Hauri et al., 2006; and Tenner et al., 2009) is applicable to our system.

The overall wet conditions of the Fresno Bench shear zones suggest that water was important for deformation. The lowest water content recorded in orthopyroxene from Fresno Bench is 180 ppm H_2O (JP10-M09), which corresponds to 20 ppm H_2O or 317 ppm H/Si in olivine. Incorporating 317 ppm H/Si in olivine results in an increase in strain rate by 1.7 orders of magnitude in dislocation creep relative to a dry sample. In diffusion creep, 317 ppm H/Si increases strain rate by a factor of 4 relative to a dry sample using the original Hirth and Kohlstedt (2003) parameters. By comparison, the maximum water content recorded in orthopyroxene is 334 ppm (JP10-M06), corresponding to 37 ppm H_2O or 588 ppm H/Si in olivine. In dislocation creep, 588 ppm H/Si in olivine results in strain rates that are 2.0 orders of magnitude higher than dry olivine and a factor of 2 higher than the minimum water estimate for Fresno Bench (317 ppm H/Si in olivine). In diffusion creep, 588 ppm H/Si in olivine leads to a strain rate that is a factor of 7 faster than a dry sample and a factor of 2 faster than olivine with 317 ppm H/Si.

As noted above, some parameters of the olivine flow laws have been updated as measurement methods have improved, such as the updated value of A by Hansen et al. (2011) for the dry diffusion creep flow law of Hirth and Kohlstedt (2003). Comparing the updated dry diffusion creep flow law to the wet diffusion creep flow law results in a strain rate contrast of 2.3 orders of magnitude for the dryest Fresno Bench sample (317 ppm H/Si) or 2.4 orders of magnitude for the

wettest sample (588 ppm H/Si). However, this comparison does not include an equivalent update for the value of A in the wet diffusion creep flow law. Using improved methods for estimating grain size, the value of A is expected to decrease and thus the strain rate contrast between the wet and dry flow laws would decrease. Uncertainty in the parameterization of different flow laws gives rise to uncertainty in the behavior of wet olivine compared to dry olivine. In Fresno Bench, however, water is present in all samples, and for the remainder of this analysis, all comparisons are done using the wet flow laws, none of which contain updated parameters.

5.4.3. Shear localization

While melt and water content both contribute to shear localization, these two factors alone cannot explain the strain gradients in the Fresno Bench shear zones. Using the maximum water content of 334 ppm in orthopyroxene combined with a 7% melt fraction, the strain rate contrast would be a factor of 17 in dislocation creep and a factor of 15 in diffusion creep, compared to a nominally melt-free sample with the minimum water content measured in the outcrop (180 ppm in orthopyroxene). However, the strain rate gradient needs to be the same order of magnitude as the strain gradient. In SZA and SZG, where maximum strains are quite high (>20, Figure 2, Table S1), the strain rate gradients calculated using melt and water (~1.2 orders of magnitude) are too low compared to this observed strain gradient (>2 orders of magnitude). Additionally, the water content for the edges of the shear zones indicate water concentrations of ~250 ppm H_2O (in orthopyroxene). Using this higher water content, the strain rate contrast between the center and the edge of the shear zones drops to a factor of ~11.

To reconcile the large strain gradients of the shear zones with the geochemical profiles we observe, other factors must have played a role in shear localization. There is no evidence for shear heating (Figure S2), and the spatial variation of pyroxene abundance does not have a direct influence on strain localization in these shear zones (for a detailed discussion, see Hansen & Warren, 2015). However, in all three shear zones, a pre-existing CPO in olivine evolves to become better-aligned with the shear direction with increasing strain (Kumamoto et al., in revision; Skemer et al., 2010; Warren et al., 2008). In a series of deformation experiments on dry, pre-textured olivine aggregates, Hansen et al. (2016) showed that viscosity could decrease by up to an order of magnitude for an aggregate with a shear-aligned CPO compared to an aggregate with a CPO aligned poorly relative to the shear direction. Modeling of the Fresno Bench shear zones by Skemer

et al. (2013) indicates that alignment of the olivine CPOs with the shear direction could lower viscosity by a factor of ~2. In addition, the higher strain shear zones (SZA and SZG) both exhibit grain size reduction in their centers. In a grain size-sensitive deformation regime, such as dislocation-accommodated grain-boundary sliding or diffusion creep, the smaller grain sizes at the centers of these two shear zones would also contribute to a locally reduced viscosity. These factors, combined with the effects of melt and water, could create the large viscosity contrasts necessary to explain the strain gradients seen in the Fresno Bench shear zones. However, both CPO realignment and grain size reduction occur after deformation has begun. Thus, while they contributed to overall shear zone formation, the initial viscosity perturbations for shear initiation must have been due to melt and water.

6. Conclusions

Small-scale shear zones like those in the Josephine Peridotite provide an opportunity to examine shear initiation and early localization in the ductile upper mantle. The Fresno Bench shear zones record a complicated history of melting, melt-rock interaction, and deformation. We propose that three stages were necessary for the formation of the Fresno Bench shear zones, based on our geochemical and microstructural observations.

1. Partial melting and depletion of the peridotite. The Fresno Bench area of the Josephine Peridotite is depleted in incompatible elements compared to source mantle. Trace element modeling indicates 16–18% partial melting is required to produce these concentrations. The lack of clinopyroxene in the Fresno Bench samples and high spinel Cr-numbers also imply a high degree of melting.

2. Channelized melt flow and shear initiation. Channelized melt flow is required to explain the observed chemical profiles, the shear zone structures, and the deformed melt structures. Initially, the melt was interstitial with an overall low melt percentage, allowing the host rock to reach equilibrium more quickly than if the channel were more dike- or vein-like. This equilibrium between the flowing melt and the host rock resulted in the observed covariation of moderately incompatible elements and water in orthopyroxene. The flow of melt through the centers of the shear zones, aided by elevated water contents in the host rock, led to a viscosity contrast between

melt-bearing and nominally melt-free regions, resulting in localization of deformation where viscosity was lower.

3. Shear localization. The presence of hydrous melt resulted in a positive feedback loop between increased melt fraction, decreased viscosity, and increased porosity (e.g., Kelemen & Dick, 1995; Stevenson, 1989) that eventually produced lithological melt channels. As strain localized in the less viscous centers of the shear zones, development of a shear-aligned crystal-preferred orientation promoted further localization (Kumamoto et al., in revision; Skemer et al., 2010, 2013; Warren et al., 2008). In SZA and SZG, grain size reduction also contributed to localization.

Acknowledgements

We thank Peter Kelemen, Greg Hirth, and Henry Dick for sharing their knowledge of the Fresno Bench shear zones; Suzanne Birner for her aid with geothermometry and measuring spinel chemistry as well as her field photography; Dale Burns and Bob Jones for their help with the microprobe; Jianhua Wang for his support with the SIMS; Suzanne Birner, Nik Deems, Megan D'Errico, Lars Hansen, Mark Kurz, and Eric Mittelstaedt for their assistance in the field; Martin Grove, Wendy Mao, and David Pollard for their comments on an early draft of this manuscript; and Ningli Zhao for the photomicrograph of 3925-G01. We also thank reviewers Roland Stalder and Nick Dygert as well as editor Uli Faul for their thoughtful reviews and constructive comments on this work. This material is based upon work supported by the National Science Foundation under grants EAR-1255620 and EAR-1625032 to J.M.W., and EAR-1806791 to K.M.K. Data supporting the analyses and conclusions are available in the supplementary material as well as from EarthChem Library at http://dx.doi.org/10.1594/IEDA/111374.

Figures

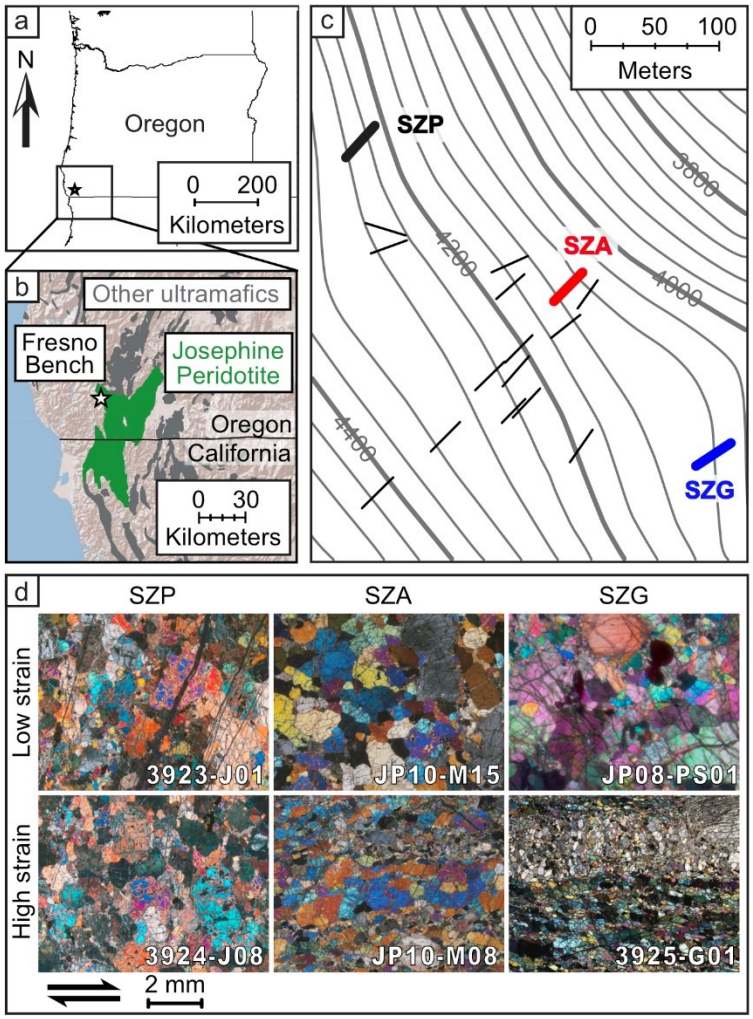

Figure 1: (**a**) The location of the Josephine Peridotite in Oregon. (**b**) The Fresno Bench outcrop (star) in the Josephine Peridotite (green). Other ultramafic units are in grey. Fresno Bench is located at 42˚10'20"N, 123˚58'53"W. After Skemer et al. (2013). (**c**) Map of the locations of shear zones on the Fresno Bench outcrop. The three analyzed shear zones are marked by bold lines, with the line orientation indicating the strike of the shear plane. Thinner black lines represent the shear planes of other shear zones in the Fresno Bench outcrop. The same length line is used to indicate the location of each shear zone and does not indicate the size of the exposure. (**d**) Photomicrographs taken under crossed polars of the lowest and highest strain samples from shear zones P, A, and G. All photomicrographs are taken at the same scale. SZA and SZG exhibit grain-size reduction in the highest strain samples, while SZP does not show any change in grain size.

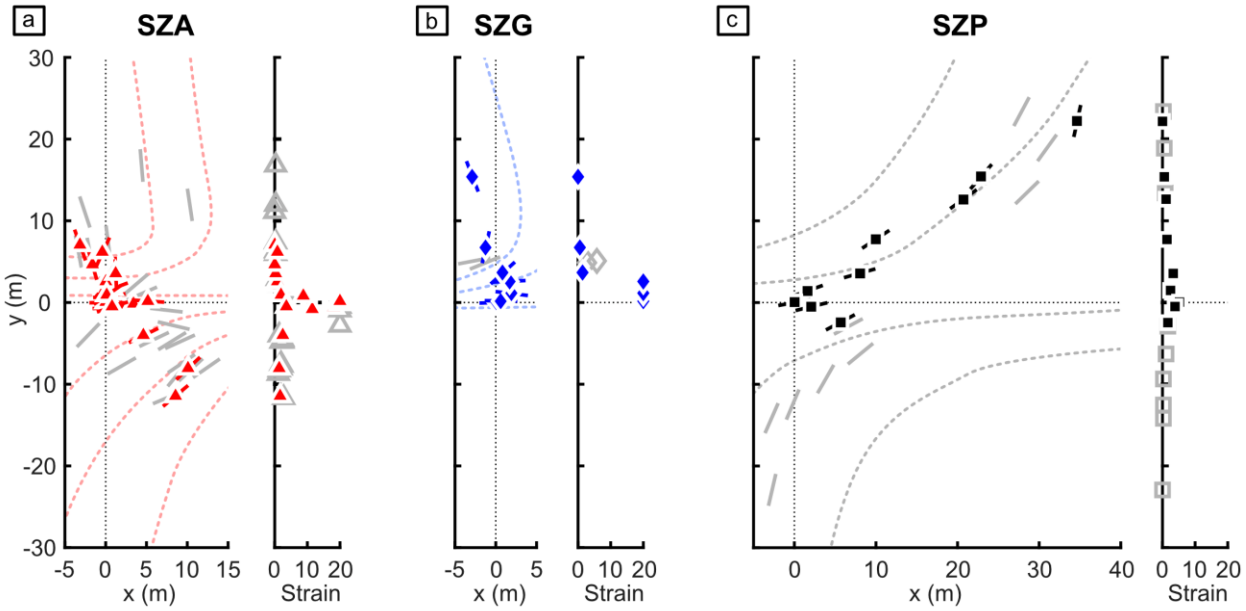

Figure 2: Structural cross-sections and strain profiles for (**a**) SZP, (**b**) SZA, and (**c**) SZG. These profiles are in the style of those presented by Skemer et al. (2010, 2013) and Warren et al. (2008), but are recalculated based on a larger set of measurements. In each structural cross-section, the x-axis is parallel to the shear direction, and the y-axis is parallel to the shear plane normal. Each foliation measurement is a grey line indicating the strike of the foliation in the structural reference frame. Foliation measurements associated with samples are colored and marked with an icon (black squares for SZP, red triangles for SZA, and blue diamonds for SZG). In the strain profiles, grey icons are associated with foliation measurements that have no corresponding sample. Strain measurements are capped at a maximum strain of 20. Black dotted lines at x = 0 and y = 0 indicate the highest strain sample of each shear zone. Dashed lines are a schematic representation of the shear zone.

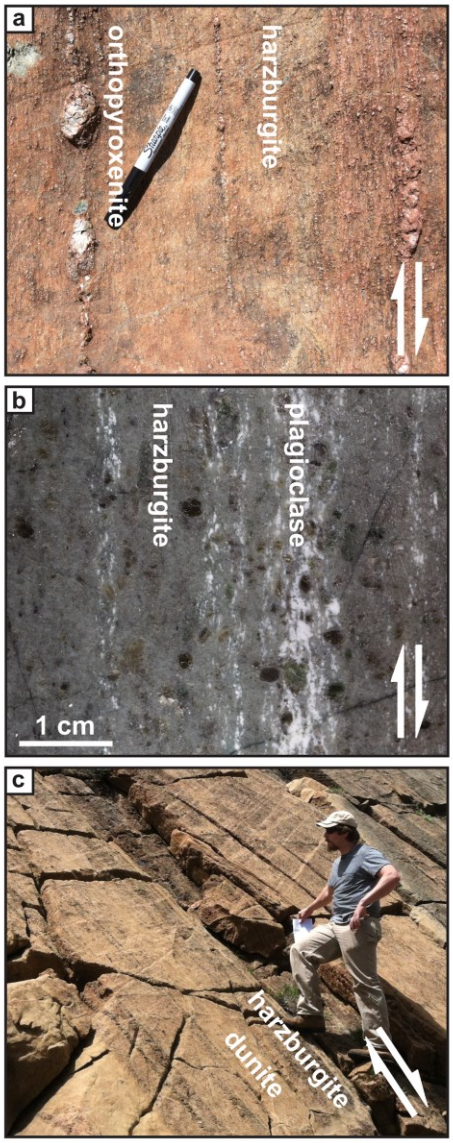

Figure 3: Lithological evidence for pre- and syn-deformational melts in the shear zones. Shear sense for each image is noted in the bottom right. (**a**) Boudinaged orthopyroxenite veins in the center of SZG. (**b**) Co-deformed, dispersed plagioclase in a sample from SZA upslope of the transect. (**c**) Dunite associated with the high-strain zone in SZP.

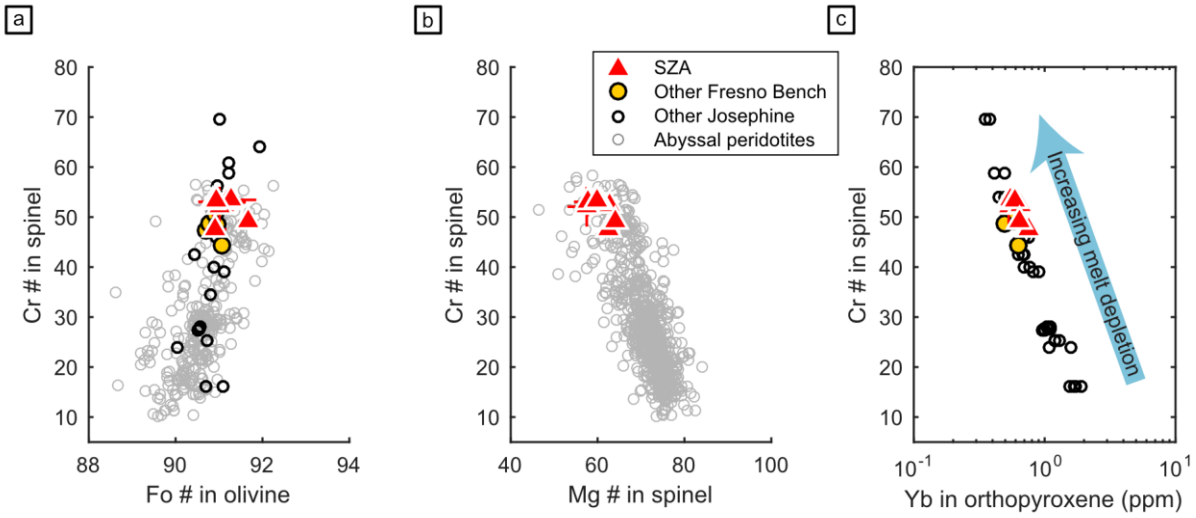

Figure 4: Compositional variations in the Fresno Bench shear zone harzburgites compared to other harzburgites from Fresno Bench (Dygert & Liang, 2015; Morgan et al., 2008), other samples from the Josephine Peridotite (Le Roux et al., 2014), and abyssal peridotites (Warren, 2016). (**a**) Spinel Cr# versus olivine Fo#. (**b**) Spinel Cr# versus spinel Mg#. Data from Morgan et al. (2008) and Le Roux et al. (2014) are not plotted as these studies did not account for ferric iron when calculating spinel Mg#. (**c**) Spinel Cr# versus Yb in orthopyroxene. Abyssal peridotites (Warren, 2016) are not shown as orthopyroxene trace elements are not available for most of these samples.

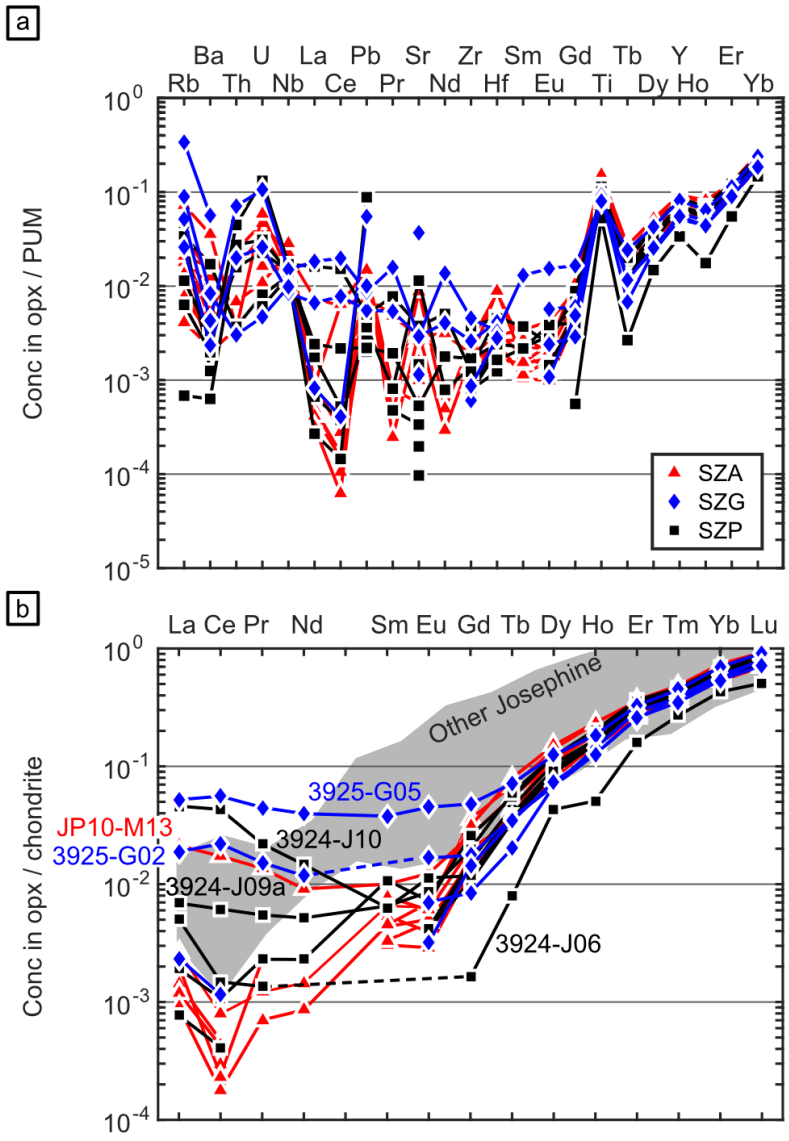

Figure 5: (**a**) Full trace element patterns for orthopyroxenes from the Fresno Bench shear zones. Concentrations are normalized to PUM (Palme & O'Neill, 2014). (**b**) Rare earth element patterns for orthopyroxenes from the Fresno Bench shear zones. Concentrations are normalized to chondrite (Anders & Grevesse, 1989). The grey field in the background represents data from Le Roux et al. (2014). In both (**a**) and (**b**), samples from SZA are red, samples from SZG are blue, and samples from SZP are black. Dashed lines are used to connect data across elements below detection for 3925-G02 and 3924-J06.

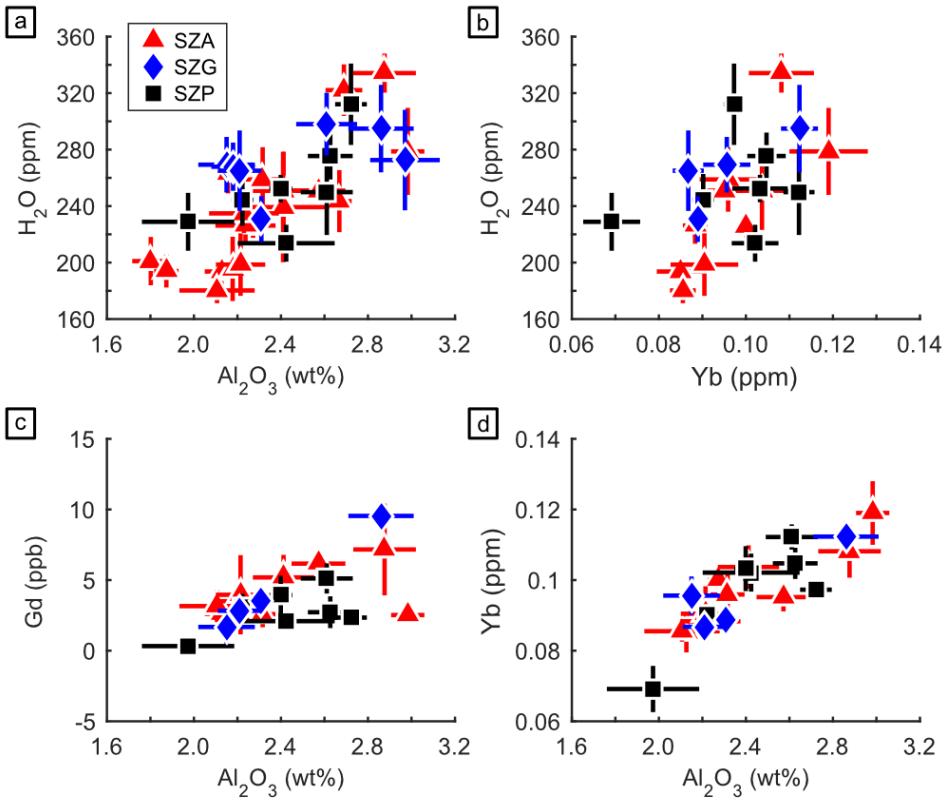

Figure 6: Covariation of elements in orthopyroxene: (**a**) Water versus alumina. (**b**) Water versus ytterbium. (**c**) Gadolinium versus alumina. (**d**) Ytterbium versus alumina.

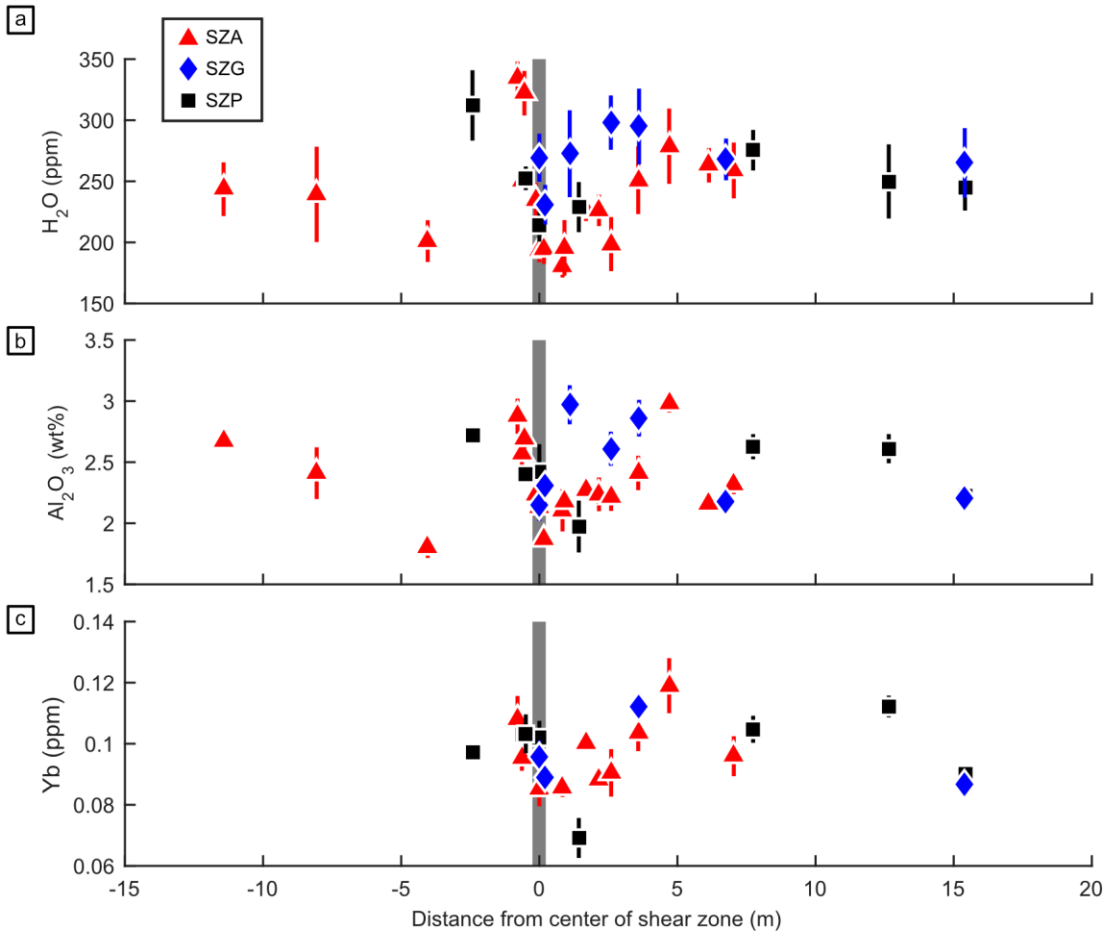

Figure 7: Transects of (**a**) water, (**b**) aluminum, and (**c**) ytterbium concentrations in orthopyroxene across the shear zones. Data are colored by shear zone. The x-axis is the same for all three plots and is the perpendicular distance from the shear plane as calculated from the structural cross-section (Table S1). The dark grey bar represents the center of the shear zone. Error bars are 1σ analytical uncertainties, and absence of an error bar represents uncertainty smaller than the marker size.

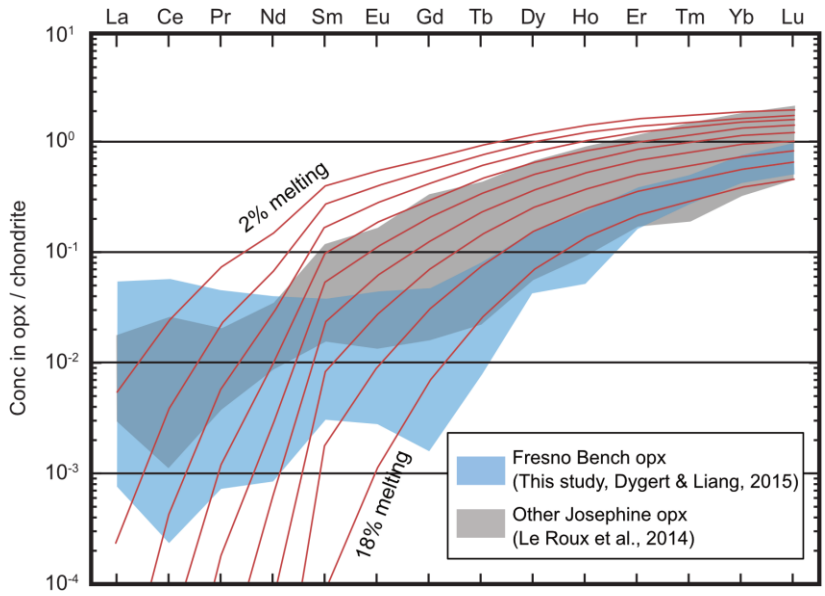

Figure 8: Comparison of Fresno Bench orthopyroxene REEs (blue shaded field; this study; Dygert & Liang, 2015) with orthopyroxene REEs from the rest of the Josephine Peridotite (grey shaded field; Le Roux et al., 2014). Red lines are contours of nonmodal fractional melting, developed from the reference model of Warren (2016) using an initial composition of Depleted MORB Mantle (Workman & Hart, 2005).

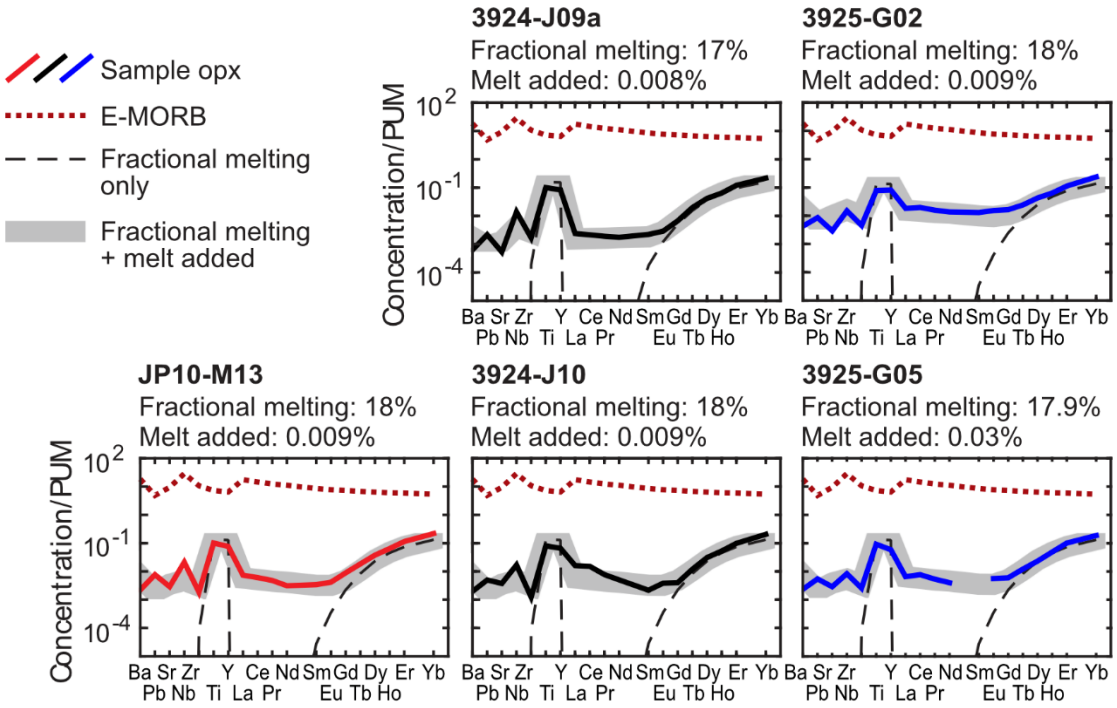

Figure 9: Simulations based on the melt refertilization model of Birner et al. (2017) for the five samples with elevated LREEs, based on fractional melting (dashed black line) followed by addition of a melt with E-MORB composition (dotted dark red line). The thick grey line represents the composition expected for fractional melting plus melt addition. The colored lines (red for SZA, black for SZP, blue for SZG) are the measured orthopyroxene compositions.

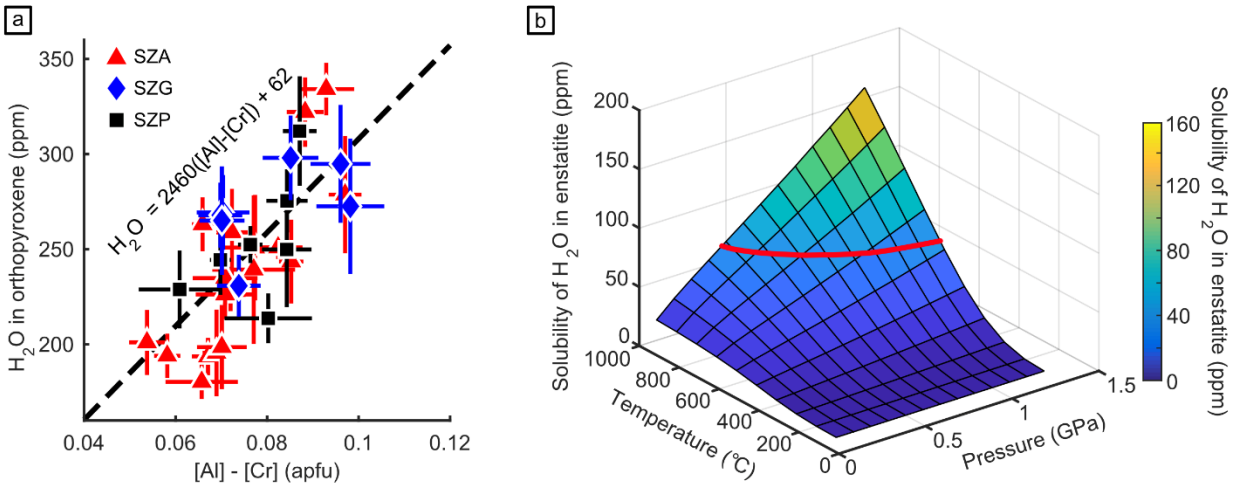

Figure 10: (**a**) Regression to calculate water in end-member enstatite. [Al] - [Cr] is the number of Al^{3+} cations per formula unit minus the number of Cr^{3+} cations per formula unit. The Al^{3+} remaining is available for charge-balancing water in a coupled substitution. The intercept of the trend in H_2O versus [Al] - [Cr] represents the amount of water that end-member enstatite can incorporate under the conditions at Fresno Bench, assuming all of the Fresno Bench orthopyroxenes are in equilibrium with each other. (**b**) The solubility of water in enstatite as a function of pressure and temperature assuming the water fugacities of Pitzer and Sterner (1994), following the equation of Rauch and Keppler (2002). The red line displays a solubility of 62 ppm H_2O in enstatite. Below this line, at lower temperatures and pressures, enstatite containing 62 ppm H_2O would be oversaturated. At higher temperatures and pressures (above the red line), enstatite containing 62 ppm H_2O would be undersaturated.

References

Anders, E., & Grevesse, N. (1989). Abundances of the elements: Meteoritic and solar. *Geochimica et Cosmochimica Acta*, *53*(1), 197–214. https://doi.org/10.1016/0016-7037(89)90286-X

Arai, S. (1987). An estimation of the least depleted spinel peridotite on the basis of olivine-spinel mantle array. *Neues Jahrbuch für Mineralogie, Monatshefte*, *8*, 347–354. https://doi.org/10.1016/0009-2541(94)90066-3

Arai, S. (1994). Characterization of spinel peridotites by olivine-spinel compositional relationships: Review and interpretation. *Chemical Geology*, *113*(3), 191–204. https://doi.org/10.1016/0009-2541(94)90066-3

Armstrong, J. T. (1988). Quantitative analysis of silicate and oxide materials: Comparison of Monte Carlo, ZAF, and φ(ρz) procedures. In D. E. Newbury (Ed.), *Microbeam Analysis* (pp. 239–246). San Francisco, CA: San Francisco Press.

Aubaud, C., Hauri, E. H., & Hirschmann, M. M. (2004). Hydrogen partition coefficients between nominally anhydrous minerals and basaltic melts. *Geophysical Research Letters*, *31*(L20611). https://doi.org/10.1029/2004GL021341

Aubaud, C., Withers, A. C., Hirschmann, M. M., Guan, Y., Leshin, L. A., Mackwell, S. J., & Bell, D. R. (2007). Intercalibration of FTIR and SIMS for hydrogen measurements in glasses and nominally anhydrous minerals. *American Mineralogist*, *92*(5-6), 811–828. https://doi.org/10.2138/am.2007.2248

Bercovici, D. (2003). The generation of plate tectonics from mantle convection. *Earth and Planetary Science Letters*, *205*(3), 107–121. https://doi.org/10.1016/S0012-821X(02)01009-9

Bercovici, D., & Ricard, Y. (2012). Mechanisms for the generation of plate tectonics by two-phase grain-damage and pinning. *Physics of the Earth and Planetary Interiors*, *202–203*, 27–55. https://doi.org/10.1016/j.pepi.2012.05.003

Birner, S. K., Warren, J. M., Cottrell, E., Davis, F. A., Kelley, K. A., & Falloon, T. J. (2017). Forearc

Peridotites from Tonga Record Heterogeneous Oxidation of the Mantle following Subduction Initiation. *Journal of Petrology*, *58*(9), 1755–1780. https://doi.org/10.1093/petrology/egx072

Bodinier, J. L., Vasseur, G., Vernieres, J., Dupuy, C., & Fabries, J. (1990). Mechanisms of Mantle Metasomatism: Geochemical Evidence from the Lherz Orogenic Peridotite. *Journal of Petrology*, *31*(3), 597–628. https://doi.org/10.1093/petrology/31.3.597

Borghini, G., Rampone, E., Zanetti, A., Class, C., Cipriani, A., Hofmann, A. W., & Goldstein, S. L. (2013). Meter-scale Nd isotopic heterogeneity in pyroxenite-bearing Ligurian peridotites encompasses global-scale upper mantle variability. *Geology*, *41*(10), 1055–1058. https://doi.org/10.1130/G34438.1

Braun, M. G., & Kelemen, P. B. (2002). Dunite distribution in the Oman Ophiolite: Implications for melt flux through porous dunite conduits. *Geochemistry, Geophysics, Geosystems*, *3*(11), 1–21. https://doi.org/10.1029/2001GC000289

Brey, G. P., & Köhler, T. (1990). Geothermobarometry in Four-phase Lherzolites II. New Thermobarometers, and Practical Assessment of Existing Thermobarometers. *Journal of Petrology*, *31*(6), 1353–1378. https://doi.org/10.1093/petrology/31.6.1353

Brunelli, D., Paganelli, E., & Seyler, M. (2014). Percolation of enriched melts during incremental open-system melting in the spinel field: A REE approach to abyssal peridotites from the Southwest Indian Ridge. *Geochimica et Cosmochimica Acta*, *127*, 190–203. https://doi.org/10.1016/j.gca.2013.11.040

Brunelli, D., Seyler, M., Cipriani, A., Ottolini, L., & Bonatti, E. (2006). Discontinuous Melt Extraction and Weak Refertilization of Mantle Peridotites at the Vema Lithospheric Section (Mid-Atlantic Ridge). *Journal of Petrology*, *47*(4), 745–771. https://doi.org/10.1093/petrology/egi092

Canil, D., & O'Neill, H. S. C. (1996). Distribution of Ferric Iron in some Upper-Mantle Assemblages. *Journal of Petrology*, *37*(3), 609–635. https://doi.org/10.1093/petrology/37.3.609

Carpenter, S. J. (2003). *The kinetics of hydrogen diffusion in single crystal orthopyroxene* (Ph.D.). Pennsylvania State University.

Chernosky, J. V., Berman, R. G., & Jenkins, D. M. (1998). The stability of tremolite: New experimental

data and a thermodynamic assessment. *American Mineralogist*, *83*(7-8), 726–739. https://doi.org/10.2138/am-1998-7-805

Chopra, P. N., & Paterson, M. S. (1984). The role of water in the deformation of dunite. *Journal of Geophysical Research*, *89*(B9), 7861–7876. https://doi.org/10.1029/JB089iB09p07861

Cooper, R. F., & Kohlstedt, D. L. (1984). Solution-precipitation enhanced diffusional creep of partially molten olivine-basalt aggregates during hot-pressing. *Tectonophysics*, *107*(3), 207–233. https://doi.org/10.1016/0040-1951(84)90252-X

Coulton, A. J., Harper, G. D., & O'Hanley, D. S. (1995). Oceanic versus emplacement age serpentinization in the Josephine ophiolite: Implications for the nature of the Moho at intermediate and slow spreading ridges. *Journal of Geophysical Research*, *100*(B11), 22245–22260. https://doi.org/10.1029/95JB02157

Davis, F. A., Cottrell, E., Birner, S. K., Warren, J. M., & Lopez, O. G. (2017). Revisiting the electron microprobe method of spinel-olivine-orthopyroxene oxybarometry applied to spinel peridotites. *American Mineralogist*, *102*(2), 421–435. https://doi.org/10.2138/am-2017-5823

Dick, H. J. B. (1976). *The origin and emplacement of the Josephine peridotite of southwestern Oregon* (Ph.D.). Yale University.

Dick, H. J. B. (1977). Partial melting in the Josephine Peridotite; I, The effect on mineral composition and its consequence for geobarometry and geothermometry. *American Journal of Science*, *277*(7), 801–832. https://doi.org/10.2475/ajs.277.7.801

Dick, H. J. B., & Bullen, T. (1984). Chromian spinel as a petrogenetic indicator in abyssal and alpine-type peridotites and spatially associated lavas. *Contributions to Mineralogy and Petrology*, *86*(1), 54–76. https://doi.org/10.1007/BF00373711

Dijkstra, A. H., Drury, M. R., Vissers, R. L. M., & Newman, J. (2002). On the role of melt-rock reaction in mantle shear zone formation in the Othris Peridotite Massif (Greece). *Journal of Structural Geology*, *24*(9), 1431–1450. https://doi.org/10.1016/S0191-8141(01)00142-0

Dixon, J. E., Leist, L., Langmuir, C., & Schilling, J.-G. (2002). Recycled dehydrated lithosphere observed in plume-influenced mid-ocean-ridge basalt. *Nature*, *420*, 385–389. https://doi.org/10.1038/nature01215

Drury, M. R., Vissers, R. L. M., Van der Wal, D., & Hoogerduijn Strating, E. H. (1991). Shear localisation in upper mantle peridotites. *Pure and Applied Geophysics*, *137*(4), 439–460. https://doi.org/10.1007/BF00879044

Dygert, N., Bernard, R. E., & Behr, W. M. (2019). Great Basin Mantle Xenoliths Record Active Lithospheric Downwelling Beneath Central Nevada. *Geochemistry, Geophysics, Geosystems*, *20*, 751–772. https://doi.org/10.1029/2018GC007834

Dygert, N., & Liang, Y. (2015). Temperatures and cooling rates recorded in REE in coexisting pyroxenes in ophiolitic and abyssal peridotites. *Earth and Planetary Science Letters*, *420*, 151–161. https://doi.org/10.1016/j.epsl.2015.02.042

Dygert, N., Liang, Y., & Kelemen, P. B. (2016). Formation of Plagioclase Lherzolite and Associated Dunite–Harzburgite–Lherzolite Sequences by Multiple Episodes of Melt Percolation and Melt–Rock Reaction: an Example from the Trinity Ophiolite, California, USA. *Journal of Petrology*, *57*(4), 815–838. https://doi.org/10.1093/petrology/egw018

Evans, B. W. (2004). The Serpentinite Multisystem Revisited: Chrysotile Is Metastable. *International Geology Review*, *46*(6), 479–506. https://doi.org/10.2747/0020-6814.46.6.479

Faul, U. H., Fitz Gerald, J. D., & Jackson, I. (2004). Shear wave attenuation and dispersion in melt-bearing olivine polycrystals: 2. Microstructural interpretation and seismological implications. *Journal of Geophysical Research: Solid Earth*, *109*(B6). https://doi.org//10.1029/2003JB002407

Faul, U. H., & Jackson, I. (2007). Diffusion creep of dry, melt-free olivine. *Journal of Geophysical Research*, *112*(B4), 59. https://doi.org/10.1029/2006JB004586

Férot, A., & Bolfan-Casanova, N. (2012). Water storage capacity in olivine and pyroxene to 14GPa: Implications for the water content of the Earth's upper mantle and nature of seismic discontinuities. *Earth and Planetary Science Letters*, *349-350*, 218–230. https://doi.org/10.1016/j.epsl.2012.06.022

Gale, A., Dalton, C. A., Langmuir, C. H., Su, Y., & Schilling, J.-G. (2013). The mean composition of ocean ridge basalts. *Geochemistry, Geophysics, Geosystems*, *14*(3), 489–518. https://doi.org/10.1029/2012GC004334

Garcia, M. O. (1982). Petrology of the Rogue River island-arc complex, Southwest Oregon. *American Journal of Science*, *282*(6), 783–807. https://doi.org/10.2475/ajs.282.6.783

Godard, M., Lagabrielle, Y., Alard, O., & Harvey, J. (2008). Geochemistry of the highly depleted peridotites drilled at ODP Sites 1272 and 1274 (Fifteen-Twenty Fracture Zone, Mid-Atlantic Ridge): Implications for mantle dynamics beneath a slow spreading ridge. *Earth and Planetary Science Letters*, *267*(3), 410–425. https://doi.org/10.1016/j.epsl.2007.11.058

Gribb, T. T., & Cooper, R. F. (2000). The effect of an equilibrated melt phase on the shear creep and attenuation behavior of polycrystalline olivine. *Geophysical Research Letters*, *27*(15), 2341–2344. https://doi.org/10.1029/2000GL011443

Handy, M. R. (1990). The solid‐state flow of polymineralic rocks. *Journal of Geophysical Research: Solid Earth*, *95*(B6), 8647–8661. https://doi.org/10.1029/JB095iB06p08647

Hansen, L. N., & Warren, J. M. (2015). Quantifying the effect of pyroxene on deformation of peridotite in a natural shear zone. *Journal of Geophysical Research: Solid Earth*, *120*(4), 2717–2738. https://doi.org/10.1002/2014JB011584

Hansen, L. N., Zimmerman, M. E., & Kohlstedt, D. L. (2011). Grain boundary sliding in San Carlos olivine: Flow law parameters and crystallographic-preferred orientation. *Journal of Geophysical Research*, *116*(B8), 149. https://doi.org/10.1029/2011JB008220

Hansen, L. N., Warren, J. M., Zimmerman, M. E., & Kohlstedt, D. L. (2016). Viscous anisotropy of textured olivine aggregates, Part 1: Measurement of the magnitude and evolution of anisotropy. *Earth and Planetary Science Letters*, *445*, 92–103. https://doi.org/10.1016/j.epsl.2016.04.008

Harding, D. J. (1988). *Josephine peridotite tectonites: A record of upper-mantle plastic flow* (Ph.D.). Cornell University.

Harper, G. D. (1984). The Josephine ophiolite, northwestern California. *GSA Bulletin*, *95*(9), 1009–1026. https://doi.org/2.0.CO;2">10.1130/0016-7606(1984)95<1009:TJONC>2.0.CO;2

Harper, G. D., Grady, K., & Coulton, A. J. (1996). Origin of the amphibolite "sole" of the Josephine ophiolite: Emplacement of a cold ophiolite over a hot arc. *Tectonics*, *15*(2), 296–313. https://doi.org/10.1029/95TC02525

Harper, G. D., Grady, K., & Wakabayashi, J. (1990). A structural study of a metamorphic sole beneath the Josephine ophiolite, western Klamath terrane, California-Oregon. In *Paleozoic and Early Mesozoic Paleogeographic Relations; Sierra Nevada, Klamath Mountains, and Related Terranes* (pp. 379–396). Geological Society of America. https://doi.org/10.1130/SPE255-p379

Hauri, E. H., Wang, J., Dixon, J. E., King, P. L., Mandeville, C., & Newman, S. (2002). SIMS analysis of volatiles in silicate glasses: 1. Calibration, matrix effects and comparisons with FTIR. *Chemical Geology*, *183*(1), 99–114. https://doi.org/10.1016/S0009-2541(01)00375-8

Hauri, E. H., Gaetani, G., & Green, T. (2006). Partitioning of water during melting of the Earth's upper mantle at H_2O-undersaturated conditions. *Earth and Planetary Science Letters*, *248*(3-4), 715–734. https://doi.org/10.1016/j.epsl.2006.06.014

Hellebrand, E., Snow, J. E., Hoppe, P., & Hofmann, A. W. (2002). Garnet-field Melting and Late-stage Refertilization in "Residual" Abyssal Peridotites from the Central Indian Ridge. *Journal of Petrology*, *43*(12), 2305–2338. https://doi.org/10.1093/petrology/43.12.2305

Hidas, K., Garrido, C. J., Tommasi, A., Padrón-Navarta, J. A., Thielmann, M., Konc, Z., et al. (2013). Strain Localization in Pyroxenite by Reaction-Enhanced Softening in the Shallow Subcontinental Lithospheric Mantle. *Journal of Petrology*, *54*(10), 1997–2031. https://doi.org/10.1093/petrology/egt039

Higgie, K., & Tommasi, A. (2012). Feedbacks between deformation and melt distribution in the crust–mantle transition zone of the Oman ophiolite. *Earth and Planetary Science Letters*, *359-360*, 61–72. https://doi.org/10.1016/j.epsl.2012.10.003

Higgie, K., & Tommasi, A. (2014). Deformation in a partially molten mantle: Constraints from

plagioclase lherzolites from Lanzo, western Alps. *Tectonophysics*, *615-616*, 167–181. https://doi.org/10.1016/j.tecto.2014.01.007

Himmelberg, G. R., & Loney, R. A. (1973). Petrology of the Vulcan Peak Alpine-Type Peridotite, Southwestern Oregon. *GSA Bulletin*, *84*(5), 1585–1600. https://doi.org/2.0.CO;2">10.1130/0016-7606(1973)84<1585:POTVPA>2.0.CO;2

Hirth, G., & Kohlstedt, D. L. (1995a). Experimental constraints on the dynamics of the partially molten upper mantle: 2. Deformation in the dislocation creep regime. *Journal of Geophysical Research*, *100*(B8), 15441–15449. https://doi.org/10.1029/95JB01292

Hirth, G., & Kohlstedt, D. L. (1995b). Experimental constraints on the dynamics of the partially molten upper mantle: Deformation in the diffusion creep regime. *Journal of Geophysical Research*, *100*(B2), 1981–2001. https://doi.org/10.1029/94JB02128

Hirth, G., & Kohlstedt, D. L. (1996). Water in the oceanic upper mantle: implications for rheology, melt extraction and the evolution of the lithosphere. *Earth and Planetary Science Letters*, *144*(1), 93–108. https://doi.org/10.1016/0012-821X(96)00154-9

Hirth, G., & Kohlstedt, D. L. (2003). Rheology of the upper mantle and the mantle wedge: A view from the experimentalists. In J. Eiler (Ed.), *Inside the Subduction Factory* (Vol. 138, pp. 83–105). https://doi.org/10.1029/138GM06

Holtzman, B. K., Groebner, N. J., Zimmerman, M. E., Ginsberg, S. B., & Kohlstedt, D. L. (2003). Stress-driven melt segregation in partially molten rocks. *Geochemistry, Geophysics, Geosystems*, *4*(5), 8607. https://doi.org/10.1029/2001GC000258

Jackson, I., Faul, U. H., Fitz Gerald, J. D., & Tan, B. H. (2004). Shear wave attenuation and dispersion in melt-bearing olivine polycrystals: 1. Specimen fabrication and mechanical testing. *Journal of Geophysical Research, [Solid Earth]*, *109*(B6). https://doi.org/10.1029/2003JB002406

Jaroslow, G. E., Hirth, G., & Dick, H. J. B. (1996). Abyssal peridotite mylonites: implications for grain-size sensitive flow and strain localization in the oceanic lithosphere. *Tectonophysics*, *256*(1), 17–37.

https://doi.org/10.1016/0040-1951(95)00163-8

Jochum, K. P., Stoll, B., Herwig, K., Willbold, M., Hofmann, A. W., Amini, M., et al. (2006). MPI-DING reference glasses for in situ microanalysis: New reference values for element concentrations and isotope ratios. *Geochemistry, Geophysics, Geosystems*, *7*(2). https://doi.org/10.1029/2005GC001060

Jochum, K. P., Willbold, M., Raczek, I., Stoll, B., & Herwig, K. (2005). Chemical Characterisation of the USGS Reference Glasses GSA-1G, GSC-1G, GSD-1G, GSE-1G, BCR-2G, BHVO-2G and BIR-1G Using EPMA, ID-TIMS, ID-ICP-MS and LA-ICP-MS. *Geostandards and Geoanalytical Research*, *29*(3), 285–302. https://doi.org/10.1111/j.1751-908X.2005.tb00901.x

Johnson, K. T. M., Dick, H. J. B., & Shimizu, N. (1990). Melting in the oceanic upper mantle: An ion microprobe study of diopsides in abyssal peridotites. *Journal of Geophysical Research*, *95*(B3), 2661. https://doi.org/10.1029/JB095iB03p02661

Kaczmarek, M.-A., & Müntener, O. (2008). Juxtaposition of Melt Impregnation and High-Temperature Shear Zones in the Upper Mantle; Field and Petrological Constraints from the Lanzo Peridotite (Northern Italy). *Journal of Petrology*, *49*(12), 2187–2220. https://doi.org/10.1093/petrology/egn065

Karato, S.-I., Paterson, M. S., & FitzGerald, J. D. (1986). Rheology of synthetic olivine aggregates: Influence of grain size and water. *Journal of Geophysical Research*, *91*(B8), 8151. https://doi.org/10.1029/JB091iB08p08151

Kelemen, P. B., & Dick, H. J. B. (1995). Focused melt flow and localized deformation in the upper mantle: Juxtaposition of replacive dunite and ductile shear zones in the Josephine peridotite, SW Oregon. *Journal of Geophysical Research*, *100*(B1), 423–438. https://doi.org/10.1029/94JB02063

Kelemen, P. B., Shimizu, N., & Salters, V. J. M. (1995). Extraction of mid-ocean-ridge basalt from the upwelling mantle by focused flow of melt in dunite channels. *Nature*, *375*, 747–753. https://doi.org/10.1038/375747a0

Kelemen, P. B., Yogodzinski, G. M., & Scholl, D. W. (2003). Along-strike variation in the Aleutian Island Arc: Genesis of high Mg# andesite and implications for continental crust. In J. Eiler (Ed.), *Inside the Subduction Factory* (Vol. 138, pp. 223–276). Washington, D. C.: American Geophysical

Union. https://doi.org/10.1029/138GM11

Keller, T., & Katz, R. F. (2016). The Role of Volatiles in Reactive Melt Transport in the Asthenosphere. *Journal of Petrology*, *57*(6), 1073–1108. https://doi.org/10.1093/petrology/egw030

Koga, K., Hauri, E. H., Hirschmann, M. M., & Bell, D. (2003). Hydrogen concentration analyses using SIMS and FTIR: Comparison and calibration for nominally anhydrous minerals. *Geochemistry, Geophysics, Geosystems*, *4*(2), 208. https://doi.org/10.1029/2002GC000378

Kohlstedt, D. L. (2006). The Role of Water in High-Temperature Rock Deformation. *Reviews in Mineralogy and Geochemistry*, *62*(1), 377–396. https://doi.org/10.2138/rmg.2006.62.16

Kovacs, I., O'Neill, H. S. C., Hermann, J., & Hauri, E. H. (2010). Site-specific infrared O-H absorption coefficients for water substitution into olivine. *American Mineralogist*, *95*(2-3), 292–299. https://doi.org/10.2138/am.2010.3313

Kruckenberg, S. C., Tikoff, B., Toy, V. G., Newman, J., & Young, L. I. (2013). Strain localization associated with channelized melt migration in upper mantle lithosphere: Insights from the Twin Sisters ultramafic complex, Washington, USA. *Journal of Structural Geology*, *50*, 133–147. https://doi.org/10.1016/j.jsg.2012.10.009

Kumamoto, K. M., Warren, J. M., & Hansen, L. N. (in revision). Evolution of the Josephine Peridotite shear zones, Part 2: Influences on olivine LPO evolution. *Journal of Geophysical Research: Solid Earth*.

Kumamoto, K. M., Warren, J. M., & Hauri, E. H. (2017). New SIMS reference materials for measuring water in upper mantle minerals. *American Mineralogist*, *102*(3), 537–547. https://doi.org/10.2138/am-2017-5863CCBYNCND

Le Roux, V., Dick, H. J. B., & Shimizu, N. (2014). Tracking flux melting and melt percolation in supra-subduction peridotites (Josephine ophiolite, USA). *Contributions to Mineralogy and Petrology*, *168*(1064). https://doi.org/10.1007/s00410-014-1064-9

Liang, Y., Sun, C., & Yao, L. (2013). A REE-in-two-pyroxene thermometer for mafic and ultramafic rocks. *Geochimica et Cosmochimica Acta*, *102*, 246–260. https://doi.org/10.1016/j.gca.2012.10.035

Li, J., Kornprobst, J., Vielzeuf, D., & Fabriès, J. (1995). An improved experimental calibration of the olivine-spinel geothermometer. *Chinese Journal of Geochemistry*, *14*(1), 68–77. https://doi.org/10.1007/BF02840385

Linckens, J., Herwegh, M., & Müntener, O. (2011). Linking temperature estimates and microstructures in deformed polymineralic mantle rocks. *Geochemistry, Geophysics, Geosystems*, *12*(8). https://doi.org/10.1029/2011GC003536

Loney, R. A., & Himmelberg, G. R. (1976). Structure of the Vulcan Peak alpine-type peridotite, southwestern Oregon. *GSA Bulletin*, *87*(2), 259–274. https://doi.org/2.0.CO;2">10.1130/0016-7606(1976)87<259:SOTVPA>2.0.CO;2

Malaspina, N., Langenhorst, F., Fumagalli, P., Tumiati, S., & Poli, S. (2012). Fe3+ distribution between garnet and pyroxenes in mantle wedge carbonate-bearing garnet peridotites (Sulu, China) and implications for their oxidation state. *Lithos*, *146-147*, 11–17. https://doi.org/10.1016/j.lithos.2012.04.023

Mei, S., Bai, W., Hiraga, T., & Kohlstedt, D. L. (2002). Influence of melt on the creep behavior of olivine-basalt aggregates under hydrous conditions. *Earth and Planetary Science Letters*, *201*, 491–507. https://doi.org/10.1016/S0012-821X(02)00745-8

Moresi, L., & Solomatov, V. (1998). Mantle convection with a brittle lithosphere: thoughts on the global tectonic styles of the Earth and Venus. *Geophysical Journal International*, *133*, 669–682. https://doi.org/10.1046/j.1365-246X.1998.00521.x

Morgan, Z., Liang, Y., & Kelemen, P. (2008). Significance of the concentration gradients associated with dunite bodies in the Josephine and Trinity ophiolites. *Geochemistry, Geophysics, Geosystems*, *9*(7). https://doi.org/10.1029/2008GC001954

Mosenfelder, J. L., & Rossman, G. R. (2013). Analysis of hydrogen and fluorine in pyroxenes: I. Orthopyroxene. *American Mineralogist*, *98*(5-6), 1026–1041. https://doi.org/10.2138/am.2013.4291

Mullen, E. K., Weis, D., Marsh, N. B., & Martindale, M. (2017). Primitive arc magma diversity: New geochemical insights in the Cascade Arc. *Chemical Geology*, *448*, 43–70.

https://doi.org/10.1016/j.chemgeo.2016.11.006

Navon, O., & Stolper, E. (1987). Geochemical Consequences of Melt Percolation: The Upper Mantle as a Chromatographic Column. *The Journal of Geology*, *95*(3), 285–307. https://doi.org/10.1086/629131

Nevitt, J. M., Warren, J. M., Kumamoto, K. M., & Pollard, D. D. (2019). Using geologic structures to constrain constitutive laws not accessible in the laboratory. *Journal of Structural Geology*, *125*, 55–63. https://doi.org/10.1016/j.jsg.2018.06.006

Palme, H., & O'Neill, H. S. C. (2014). Cosmochemical Estimates of Mantle Composition. In H. D. Holland & K. K. Turekian (Eds.), *Treatise on Geochemistry (Second Edition)* (pp. 1–39). Oxford: Elsevier. https://doi.org/10.1016/B978-0-08-095975-7.00201-1

Peslier, A. H. (2010). A review of water contents of nominally anhydrous natural minerals in the mantles of Earth, Mars and the Moon. *Journal of Volcanology and Geothermal Research*, *197*(1), 239–258. https://doi.org/10.1016/j.jvolgeores.2009.10.006

Pitzer, K. S., & Sterner, S. M. (1994). Equations of state valid continuously from zero to extreme pressures for H 2 O and CO 2. *The Journal of Chemical Physics*, *101*(4), 3111–3116. https://doi.org/10.1063/1.467624

Plank, T., Kelley, K. A., Zimmer, M. M., Hauri, E. H., & Wallace, P. J. (2013). Why do mafic arc magmas contain ~4wt% water on average? *Earth and Planetary Science Letters*, *364*, 168–179. https://doi.org/10.1016/j.epsl.2012.11.044

Prechtel, F., & Stalder, R. (2012). OH-defects in Al- and Cr- doped synthetic enstatites and defect geobarometry on natural orthopyroxenes from the Earth's mantle. *European Journal of Mineralogy*, *24*(3), 471–481. https://doi.org/10.1127/0935-1221/2012/0024-2208

Précigout, J., Prigent, C., Palasse, L., & Pochon, A. (2017). Water pumping in mantle shear zones. *Nature Communications*, *8*, 15736. https://doi.org/10.1038/ncomms15736

Ramsay, J. G. (1980). Shear zone geometry: A review. *Journal of Structural Geology*, *2*(1), 83–99. https://doi.org/10.1016/0191-8141(80)90038-3

Ramsay, J. G., & Graham, R. H. (1970). Strain variation in shear belts. *Canadian Journal of Earth*

Sciences, *7*(3), 786–813. https://doi.org/10.1139/e70-078

Rauch, M., & Keppler, H. (2002). Water solubility in orthopyroxene. *Contributions to Mineralogy and Petrology*, *143*(5), 525–536. https://doi.org/10.1007/s00410-002-0365-6

Recanati, A., Kurz, M. D., Warren, J. M., & Curtice, J. (2012). Helium distribution in a mantle shear zone from the Josephine Peridotite. *Earth and Planetary Science Letters*, *359-360*, 162–172. https://doi.org/10.1016/j.epsl.2012.09.046

Regenauer-Lieb, K., Yuen, D. A., & Branlund, J. (2001). The initiation of subduction: criticality by addition of water? *Science*, *294*(5542), 578–580. https://doi.org/10.1126/science.1063891

Saleeby, J. B., Harper, G. D., Snoke, A. W., & Sharp, W. D. (1982). Time relations and structural-stratigraphic patterns in ophiolite accretion, west central Klamath Mountains, California. *Journal of Geophysical Research*, *87*(B5), 3831. https://doi.org/10.1029/JB087iB05p03831

Schwartz, S., Guillot, S., Reynard, B., Lafay, R., Debret, B., Nicollet, C., et al. (2013). Pressure–temperature estimates of the lizardite/antigorite transition in high pressure serpentinites. *Lithos*, *178*, 197–210. https://doi.org/10.1016/j.lithos.2012.11.023

Skemer, P., Warren, J. M., Hansen, L. N., Hirth, G., & Kelemen, P. B. (2013). The influence of water and LPO on the initiation and evolution of mantle shear zones. *Earth and Planetary Science Letters*, *375*, 222–233. https://doi.org/10.1016/j.epsl.2013.05.034

Skemer, P., Warren, J. M., Kelemen, P. B., & Hirth, G. (2010). Microstructural and Rheological Evolution of a Mantle Shear Zone. *Journal of Petrology*, *51*(1-2), 43–53. https://doi.org/10.1093/petrology/egp057

Sonzogni, Y., Treiman, A. H., & Schwenzer, S. P. (2017). Serpentinite with and without brucite: A reaction pathway analysis of a natural serpentinite in the Josephine ophiolite, California. *Journal of Mineralogical and Petrological Sciences*, *112*(2), 59–76. https://doi.org/10.2465/jmps.160509

Spiegelman, M., & Kelemen, P. B. (2003). Extreme chemical variability as a consequence of channelized melt transport. *Geochemistry, Geophysics, Geosystems*, *4*(7), 20,433. https://doi.org/10.1029/2002GC000336

Spiegelman, M., Kelemen, P. B., & Aharonov, E. (2001). Causes and consequences of flow organization during melt transport: The reaction infiltration instability in compactible media. *Journal of Geophysical Research*, *106*(B2), 2061–2077. https://doi.org/10.1029/2000JB900240

Stalder, R. (2004). Influence of Fe, Cr and Al on hydrogen incorporation in orthopyroxene. *European Journal of Mineralogy*, *16*(5), 703–711. https://doi.org/10.1127/0935-1221/2004/0016-0703

Stalder, R., & Behrens, H. (2006). D/H exchange in pure and Cr-doped enstatite: implications for hydrogen diffusivity. *Physics and Chemistry of Minerals*, *33*(8), 601–611. https://doi.org/10.1007/s00269-006-0112-z

Stalder, R., Karimova, A., & Konzett, J. (2015). OH-defects in multiple-doped orthoenstatite at 4–8 GPa: filling the gap between pure and natural systems. *Contributions to Mineralogy and Petrology*, *169*(4), 38. https://doi.org/10.1007/s00410-015-1133-8

Stalder, R., Klemme, S., Ludwig, T., & Skogby, H. (2005). Hydrogen incorporation in orthopyroxene: interaction of different trivalent cations. *Contributions to Mineralogy and Petrology*, *150*(5), 473–485. https://doi.org/10.1007/s00410-005-0037-4

Stalder, R., & Skogby, H. (2002). Hydrogen incorporation in enstatite. *European Journal of Mineralogy*, *14*(6), 1139–1144. https://doi.org/10.1127/093512202761673439

Stalder, R., & Skogby, H. (2003). Hydrogen diffusion in natural and synthetic orthopyroxene. *Physics and Chemistry of Minerals*, *30*(1), 12–19. https://doi.org/10.1007/s00269-002-0285-z

Stevenson, D. J. (1989). Spontaneous small-scale melt segregation in partial melts undergoing deformation. *Geophysical Research Letters*, *16*(9), 1067–1070. https://doi.org/10.1029/GL016i009p01067

Suhr, G., Hellebrand, E., Snow, J. E., Seck, H. A., & Hofmann, A. W. (2003). Significance of large, refractory dunite bodies in the upper mantle of the Bay of Islands Ophiolite. *Geochemistry, Geophysics, Geosystems*, *4*(3), 1. https://doi.org/10.1029/2001GC000277

Sun, C., & Liang, Y. (2014). An assessment of subsolidus re-equilibration on REE distribution among mantle minerals olivine, orthopyroxene, clinopyroxene, and garnet in peridotites. *Chemical Geology*,

372, 80–91. https://doi.org/10.1016/j.chemgeo.2014.02.014

Tackley, P. J. (1998). Self-consistent generation of tectonic plates in three-dimensional mantle convection. *Earth and Planetary Science Letters*, *157*(1), 9–22. https://doi.org/10.1016/S0012-821X(98)00029-6

Tenner, T. J., Hirschmann, M. M., Withers, A. C., & Hervig, R. L. (2009). Hydrogen partitioning between nominally anhydrous upper mantle minerals and melt between 3 and 5 GPa and applications to hydrous peridotite partial melting. *Chemical Geology*, *262*(1), 42–56. https://doi.org/10.1016/j.chemgeo.2008.12.006

Tollan, P. M. E., O'Neill, H. S. C., & Hermann, J. (2018). The role of trace elements in controlling H incorporation in San Carlos olivine. *Contributions to Mineralogy and Petrology. Beitrage Zur Mineralogie Und Petrologie*, *173*(11), 89. https://doi.org/10.1007/s00410-018-1517-7

Tommasi, A., Knoll, M., Vauchez, A., Signorelli, J. W., Thoraval, C., & Logé, R. (2009). Structural reactivation in plate tectonics controlled by olivine crystal anisotropy. *Nature Geoscience*, *2*, 423. https://doi.org/10.1038/ngeo528

Trompert, R., & Hansen, U. (1998). Mantle convection simulations with rheologies that generate plate-like behaviour. *Nature*, *395*, 686. https://doi.org/10.1038/27185

Trouw, R. A. J., Passchier, C. W., & Wiersma, D. J. (2009). *Atlas of Mylonites- and related microstructures*. https://doi.org/10.1007/978-3-642-03608-8

Vernières, J., Godard, M., & Bodinier, J.-L. (1997). A plate model for the simulation of trace element fractionation during partial melting and magma transport in the Earth's upper mantle. *Journal of Geophysical Research*, *102*(B11), 24771–24784. https://doi.org/10.1029/97JB01946

Wang, C., Liang, Y., Dygert, N., & Xu, W. (2016). Formation of orthopyroxenite by reaction between peridotite and hydrous basaltic melt: an experimental study. *Contributions to Mineralogy and Petrology*, *171*(77). https://doi.org/10.1007/s00410-016-1287-z

Warren, J. M. (2016). Global variations in abyssal peridotite compositions. *Lithos*, *248-251*, 193–219. https://doi.org/10.1016/j.lithos.2015.12.023

Warren, J. M., & Hauri, E. H. (2014). Pyroxenes as tracers of mantle water variations. *Journal of Geophysical Research: Solid Earth*, *119*(3), 1851–1881. https://doi.org/10.1002/2013JB010328

Warren, J. M., Hirth, G., & Kelemen, P. B. (2008). Evolution of olivine lattice preferred orientation during simple shear in the mantle. *Earth and Planetary Science Letters*, *272*(3), 501–512. https://doi.org/10.1016/j.epsl.2008.03.063

Withers, A. C., Hirschmann, M. M., & Tenner, T. J. (2011). The effect of Fe on olivine H_2O storage capacity: Consequences for H_2O in the martian mantle. *American Mineralogist*, *96*(7), 1039–1053. https://doi.org/10.2138/am.2011.3669

Witt-Eickschen, G., & Seck, H. A. (1991). Solubility of Ca and AI in orthopyroxene from spinel peridotite: an improved version of an empirical geothermometer. *Contributions to Mineralogy and Petrology*, *106*, 431–439. https://doi.org/10.1007/BF00321986

Workman, R. K., & Hart, S. R. (2005). Major and trace element composition of the depleted MORB mantle (DMM). *Earth and Planetary Science Letters*, *231*(1), 53–72. https://doi.org/10.1016/j.epsl.2004.12.005